J|A|C|S
ARTICLES

Published on Web 07/22/2010

# Self-Assembly of Hybrid Dendrons into Doubly Segregated Supramolecular Polyhedral Columns and Vesicles

Mihai Peterca,†,‡ Mohammad R. Imam,†,§ Pawaret Leowanawat,† Brad M. Rosen,†
Daniela A. Wilson,† Christopher J. Wilson,† Xiangbing Zeng,‖ Goran Ungar,‖
Paul A. Heiney,‡ and Virgil Percec*,†

*Roy & Diana Vagelos Laboratories, Department of Chemistry, and Department of Physics and Astronomy, University of Pennsylvania, Philadelphia, Pennsylvania 19104, and Department of Engineering Materials, University of Sheffield, Sheffield S1 3JD, United Kingdom*

Received May 21, 2010; E-mail: percec@sas.upenn.edu

***Abstract:*** The synthesis and structural analysis of supramolecular dendrimers self-assembled from 3 libraries containing 20 first-generation hybrid dendrons are reported. Combinations of benzyl ether, naphthyl methyl ether, and biphenyl methyl ether repeat units with different alkyl carboxylates at the apex of the dendron decreased its molecular solid angle to values that led to the discovery of a new mechanism of self-assembly. This new self-assembly mechanism generated a diversity of unprecedented supramolecular assemblies, including hollow and nonhollow singly or doubly segregated supramolecular columns and vesicles exhibiting polyhedral shapes. The polyhedral shape of the self-organized supramolecular dendrimers was demonstrated to be an intrinsic characteristic of all the doubly segregated structures. The self-assembly mechanism elucidated here provides access to new strategies that will be used to fabricate complex supramolecular organizations.

## 1. Introduction

Self-assembling dendrons[1] and dendrimers,[2] synthesized via iterative convergent,[3] divergent,[4] or combined methodologies, are monodisperse macromolecules that form a variety of complex periodic or quasi-periodic spatial organizations.[5] These organizations are determined by their specific primary structure and are dependent on the environmental conditions. Self-assembling dendritic structures have impacted the field of supramolecular nanoscience[6] with applications ranging from supramolecular capsules,[7] vesicles,[8] porous protein mimics,[9] and ion channels[10] to molecular actuators[11] and organic electronic materials.[12] Establishing general principles that correlate the dendritic primary structure with the resulting supramolecular structure in the self-organized state is essential not only for the design of building blocks that provide new functions, but also

---

† Department of Chemistry, University of Pennsylvania.

‡ Department of Physics and Astronomy, University of Pennsylvania.

§ Current address: Department of Chemistry, King Fahd University of Petroleum & Minerals (KFUPM), Dhahran 31261, Saudi Arabia.

‖ University of Sheffield.

(1) (a) Balagurusamy, V. S. K.; Ungar, G.; Percec, V.; Johansson, G. *J. Am. Chem. Soc.* **1997**, *119*, 1539–1555. (b) Percec, V.; Cho, W. D.; Ungar, G.; Yeardley, D. J. P. *J. Am. Chem. Soc.* **2001**, *123*, 1302–1315. (c) Zubarev, E. R.; Pralle, M. U.; Sone, E. D.; Stupp, S. I. *J. Am. Chem. Soc.* **2002**, *123*, 4105–4106. (d) Percec, V.; Mitchell, C. M.; Cho, W. D.; Uchida, S.; Glodde, M.; Ungar, G.; Zeng, X. B.; Liu, Y. S.; Balagurusamy, V. S. K.; Heiney, P. A. *J. Am. Chem. Soc.* **2004**, *126*, 6078–6094. (e) Kim, J. K.; Hong, M. K.; Ahn, J. H.; Lee, M. *Angew. Chem., Int. Ed.* **2005**, *44*, 328–332. (f) Sakai, N.; Kamikawa, Y.; Nishii, M.; Matsuoka, T.; Kato, T.; Matile, S. *J. Am. Chem. Soc.* **2006**, *128*, 2218–2219. (g) Percec, V.; Peterca, M.; Sienkowska, M. J.; Ilies, M. A.; Aqad, E.; Smidrkal, J.; Heiney, P. A. *J. Am. Chem. Soc.* **2006**, *128*, 3324–3334. (h) Percec, V.; Holerca, M. N.; Nummelin, S.; Morrison, J. L.; Glodde, M.; Smidrkal, J.; Peterca, M.; Rosen, B. M.; Uchida, S.; Balagurusamy, V. S. K.; Sienkowska, M. J.; Heiney, P. A. *Chem.—Eur. J.* **2006**, *12*, 6216–6241. (i) Percec, V.; Won, B. C.; Peterca, M.; Heiney, P. A. *J. Am. Chem. Soc.* **2007**, *129*, 11265–11278. (j) Zhang, X.; Chen, Z.; Würthner, F. *J. Am. Chem. Soc.* **2007**, *129*, 4886–4887. (k) Gehringer, L.; Bourgogne, C.; Guillon, D.; Donnio, B. *J. Am. Chem. Soc.* **2004**, *126*, 3856–3867. (l) Cook, A. G.; Baumeister, U.; Tschierske, C. *J. Mater. Chem.* **2005**, *15*, 1708–1721. (m) Bury, I.; Heinrich, B.; Bourgogne, C.; Guillon, D.; Donnio, B. *Chem.—Eur. J.* **2006**, *12*, 8396–8413. (n) Lehmann, M.; Jahr, M. *Chem. Mater.* **2008**, *20*, 5453–5456. (o) Lee, M.; Jeong, Y. S.; Cho, B. K.; Oh, N. K.; Zin, W. C. *Chem.—Eur. J.* **2002**, *8*, 876–883. (p) Cho, B. K.; Jain, A.; Gruner, S. M.; Wiesner, U. *Science* **2004**, *305*, 1598–1601. (q) Peterca, M.; Percec, V.; Imam, M. R.; Leowanawat, P.; Morimitsu, K.; Heiney, P. A. *J. Am. Chem. Soc.* **2008**, *130*, 14840–14852. (r) Dukeson, D. R.; Ungar, G.; Balagurusamy, V. S. K.; Percec, V.; Johansson, G. A.; Glodde, M. *J. Am. Chem. Soc.* **2003**, *125*, 15974–15980. (s) Percec, V.; Peterca, M.; Tsuda, Y.; Rosen, B. M.; Uchida, S.; Imam, M. R.; Ungar, G.; Heiney, P. A. *Chem.—Eur. J.* **2009**, *15*, 8994–9004. (t) Percec, V.; Rudick, J. G.; Peterca, M.; Yurchenko, M. E.; Smidrkal, J.; Heiney, P. A. *Chem.—Eur. J.* **2008**, *14*, 3355–3362.

(2) (a) Fréchet, J. M. J., Tomalia, D. A., Eds. *Dendrimers and Other Dendritic Polymers*; Wiley: New York, 2001. (b) Newkome, G. R.; Moorefield, C. N.; Vögtle, F. *Dendrimers and Dendrons*; Wiley-VCH: Weinheim, Germany, 2001. (c) Vögtle, F.; Richardt, G.; Werner, N. *Dendrimer Chemistry*; Wiley-VCH: Weinheim, Germany, 2009.

(3) (a) Hawker, C. J.; Fréchet, J. M. J. *J. Am. Chem. Soc.* **1990**, *112*, 7638–7647. (b) Miller, T. M.; Neenan, T. X. *Chem. Mater.* **1990**, *2*, 346–349. (c) Grayson, S. M.; Fréchet, J. M. J. *Chem. Rev.* **2001**, *101*, 3819–3868.

(4) (a) Buhleier, E.; Wehner, W.; Vögtle, F. *Synthesis* **1978**, *15*, 5–158. (b) Tomalia, D. A.; Baker, H.; Dewald, J.; Hall, M.; Kallos, G.; Martin, S.; Roeck, J.; Ryder, J.; Smith, P. *Polym. J.* **1985**, *17*, 117–132. (c) Newkome, G. R.; Yao, Z.; Baker, G. R.; Gupta, V. K. *J. Org. Chem.* **1985**, *50*, 2003–2004.

(5) Rosen, B. M.; Wilson, C. J.; Wilson, D. A.; Peterca, M.; Imam, M. R.; Percec, V. *Chem. Rev.* **2009**, *109*, 6275–6540.

(6) For selected reviews on supramolecular liquid crystalline dendrimers see: (a) Moore, J. S. *Acc. Chem. Res.* **1997**, *30*, 402–413. (b) Ponomarenko, S. A.; Boiko, N. I.; Shibaev, V. P. *Polym. Sci., Ser. C* **2001**, *43*, 1–45. (c) Donnio, B.; Guillon, D. *Adv. Poylm. Sci.* **2006**, *201*, 45–155. (d) Caminade, A. M.; Turrin, C. O.; Sutra, P.; Majoral, J. P. *Curr. Opin. Colloid Interface Sci.* **2003**, *8*, 282–295. (e) Deschenaux, R.; Donnio, B.; Guillon, D. *New J. Chem.* **2007**, *31*, 1064–1073. (f) Marcos, M.; Martin-Rapun, R.; Omenat, A.; Serrano, J. L. *Chem. Soc. Rev.* **2007**, *36*, 1889–1901. (g) Rudick, J. G.; Percec, V. *Acc. Chem. Res.* **2008**, *41*, 1641–1652. (h) Rudick, J. G.; Percec, V. *New J. Chem.* **2007**, *31*, 1083–1096. (i) Ungar, G.; Zeng, X. B. *Soft Matter* **2005**, *1*, 95–106.

**10.1021/ja104432d**

***Scheme 1.*** Synthesis of Periphery Groups of the Hybrid Dendrons

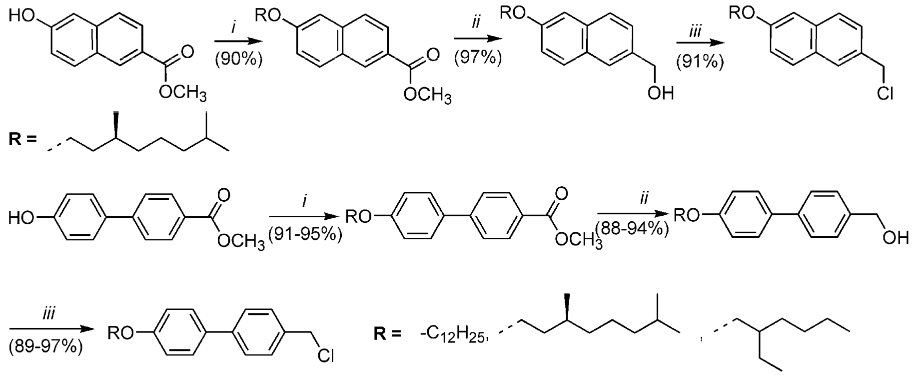

Reactions and Conditions: (i) R-Br, $K_2CO_3$, DMF, 80 °C; (ii) $LiAlH_4$, THF, 0 °C-RT; (iii) $SOCl_2$, DMF (cat.), $CH_2Cl_2$, 0 °C-RT.

for the understanding of similar organizations observed in biological structures.[13]

Classes of dendritic structures were recently shown to self-assemble into bicontinuous cubic phases,[14] triple-network cubic phases,[15] supramolecular porous columns,[9] and hollow spheres[7c] with a hollow center ranging from a few angstroms to a few nanometers. The formation of hollow supramolecular assemblies was correlated with the decrease of the solid angle of the dendron.[7c,9] On the other hand, the process of self-assembly of dendritic structures into a variety of bicontinuous cubic phases is not well understood. This process was mostly correlated with the primary structure of the self-assembling dendron.[5,16,17] Encapsulation and selective transport of larger molecular guests require a further increase of the size of the hollow regions. Considering that these empty regions can have a significant penalty to the value of the free energy, constructing larger hollow centers is problematic. Furthermore, increasing the size and complexity of the supramolecular assemblies, without increasing the complexity of the building block, represents a considerable challenge. Here we report the engineering of the solid angle of the dendron[16] through the synthesis of first-generation hybrid self-assembling dendrons based on combinations of benzyl ether, naphthyl methyl ether, and biphenyl methyl ether repeat units and different alkyl carboxylates at the apex.

Using reconstruction of the electron density distributions and analysis and simulation of the powder X-ray diffractograms, in combination with molecular modeling, we establish that the self-assembly of dendrons follows either the traditional singly segregated aliphatic−aromatic route[1,5] or a new doubly segregated aliphatic−aromatic−aliphatic route.[17] The differentiation between the two pathways followed by the self-assembly process is correlated with the dendron solid angle, the structure of the apex building block, and the addition of branching points in the alkyl chains. New methodologies based on the analytical calculation of the Fourier transform of the polyhedral domains were developed to facilitate complete structural analysis of the singly and doubly segregated columnar phases. For the cubic phases, the powder X-ray data simulations involved numerical multidimensional integration over polyhedral domains generated by a new method called “scaled Voronoi tessellation”. This method is general and can be easily modified to simulate X-ray powder diffractions of any other type of polyhedral domain. New structural characterization techniques were also developed to calculate the number of dendrons forming the inner and outer layers of the doubly segregated assemblies. The dependence

---

(7) (a) Ryu, J.-H.; Lee, E.; Lim, Y.-B.; Lee, M. *J. Am. Chem. Soc.* **2007**, *129*, 4808–4814. (b) Li, B.; Martin, A. L.; Gillies, E. R. *Chem. Commun.* **2007**, 5217–5219. (c) Percec, V.; Peterca, M.; Dulcey, A. E.; Imam, M. R.; Hudson, S. D.; Nummelin, S.; Adelman, P.; Heiney, P. A. *J. Am. Chem. Soc.* **2008**, *130*, 13079–13094. (d) Park, C.; Lim, J.; Yun, M.; Kim, C. *Angew. Chem., Int. Ed.* **2008**, *47*, 2959–2969. (e) Zhang, X.; Rehm, S.; Safont-Sempere, M. M.; Würthner, F. *Nat. Chem.* **2009**, *1*, 623–629.

(8) Percec, V.; et al. *Science* **2010**, *328*, 1009–1014.

(9) (a) Percec, V.; Dulcey, A. E.; Balagarusamy, V. S. K.; Miura, Y.; Smidrkal, J.; Peterca, M.; Nummelin, S.; Hudson, S. D.; Heiney, P. A.; Duan, H.; Magonov, S. N.; Vinogradov, S. A. *Nature* **2004**, *430*, 764–769. (b) Percec, V.; Dulcey, A. E.; Peterca, M.; Ilies, M.; Ladislaw, J.; Rosen, B. M.; Edlund, U.; Heiney, P. A. *Angew. Chem., Int. Ed.* **2005**, *44*, 6516–6521. (c) Percec, V.; Dulcey, A. E.; Peteca, M.; Ilies, M.; Miura, Y.; Edlund, Y.; Heiney, P. A. *Aust. J. Chem.* **2005**, *58*, 472–482. (d) Percec, V.; Dulcey, A. E.; Peterca, M.; Ilies, M.; Sienkowska, M. J.; Heiney, P. A. *J. Am. Chem. Soc.* **2005**, *127*, 17902–17909. (e) Percec, V.; Dulcey, A. E.; Peterca, M.; Ilies, M.; Nummelin, S.; Sienkowska, M. J.; Heiney, P A. *Proc. Natl. Acad. Sci. U.S.A.* **2006**, *103*, 2518–2523. (f) Peterca, M.; Percec, V.; Dulcey, A. E.; Nummelin, S.; Korey, S.; Ilies, M.; Heiney, P. A. *J. Am. Chem. Soc.* **2006**, *128*, 6713–6720. (g) Percec, V.; Dulcey, A. E.; Peterca, M.; Adelman, P.; Samant, R.; Balagurusamy, V. S. K.; Heiney, P. A. *J. Am. Chem. Soc.* **2007**, *129*, 5992–6002. (h) Kaucher, M. S.; Peterca, M.; Dulcey, A. E.; Kim, A. J.; Vinogradov, S. A.; Hammer, D. A.; Heiney, P. A.; Percec, V. *J. Am. Chem. Soc.* **2007**, *129*, 11698–11699.

(10) Sakai, N.; Kamikawa, Y.; Nishii, M.; Matsuoka, T.; Kato, T.; Matile, S. *J. Am. Chem. Soc.* **2006**, *128*, 2218–2219.

(11) Percec, V.; Rudick, J. G.; Peterca, M.; Heiney, P. A. *J. Am. Chem. Soc.* **2008**, *130*, 7503–7508.

(12) (a) Gilat, S. L.; Andronov, A.; Fréchet, J. M. J. *Angew. Chem., Int. Ed.* **1999**, *38*, 1422–1427. (b) Schenning, A. P. H. J.; Peeters, E.; Meijer, E. W. *J. Am. Chem. Soc.* **2000**, *122*, 4489–4495. (c) Maus, M.; De, R.; Lor, M.; Weil, T.; Mitra, S.; Wiesler, U.-M.; Herrmann, A.; Hofkens, J.; Vosch, T.; Müllen, K.; De Schryver, F. C. *J. Am. Chem. Soc.* **2001**, *123*, 7668–7676. (d) Percec, V.; Glodde, M.; Bera, T. K.; Miura, Y.; Shiyanovskaya, I.; Singer, K. D.; Balagurusamy, V. S. K.; Heiney, P. A.; Schnell, I.; Rapp, A.; Spiess, H. W.; Hudson, S. D.; Duan, H. *Nature* **2002**, *419*, 384–387. (e) Messmore, B. W.; Hulvat, J. F.; Sone, E. D.; Stupp, S. I. *J. Am. Chem. Soc.* **2004**, *126*, 14452–14458. (f) Cho, B. K.; Jain, A.; Gruner, S. M.; Wiesner, U. *Chem. Commun.* **2005**, 2143–2145. (g) Sagara, Y.; Kato, T. *Angew. Chem., Int. Ed.* **2008**, *47*, 5175–5178. (h) Miyajima, D.; Tashuiro, K.; Araoka, F.; Takazoe, H.; Kim, J.; Kato, K.; Takata, M.; Aida, T. *J. Am. Chem. Soc.* **2009**, *131*, 44–45.

(13) (a) Seifert, U. *Adv. Phys.* **1997**, *46*, 13–137. (b) Miyazawa, A.; Fujiyoshi, Y.; Unwin, N. *Nature* **2003**, *423*, 949–955.

(14) Chvalun, S. N.; Shcherbina, M. A.; Yakunin, A. N.; Blackwell, J.; Percec, V. *Polym. Sci., Ser. A* **2007**, *49*, 158–167.

(15) Rosen, B. M.; Peterca, M.; Huang, C.; Zeng, X. B.; Ungar, G.; Percec, V., *Angew. Chem., Int. Ed.*, in press.

***Scheme 2.*** Synthesis of Hybrid Dendrons

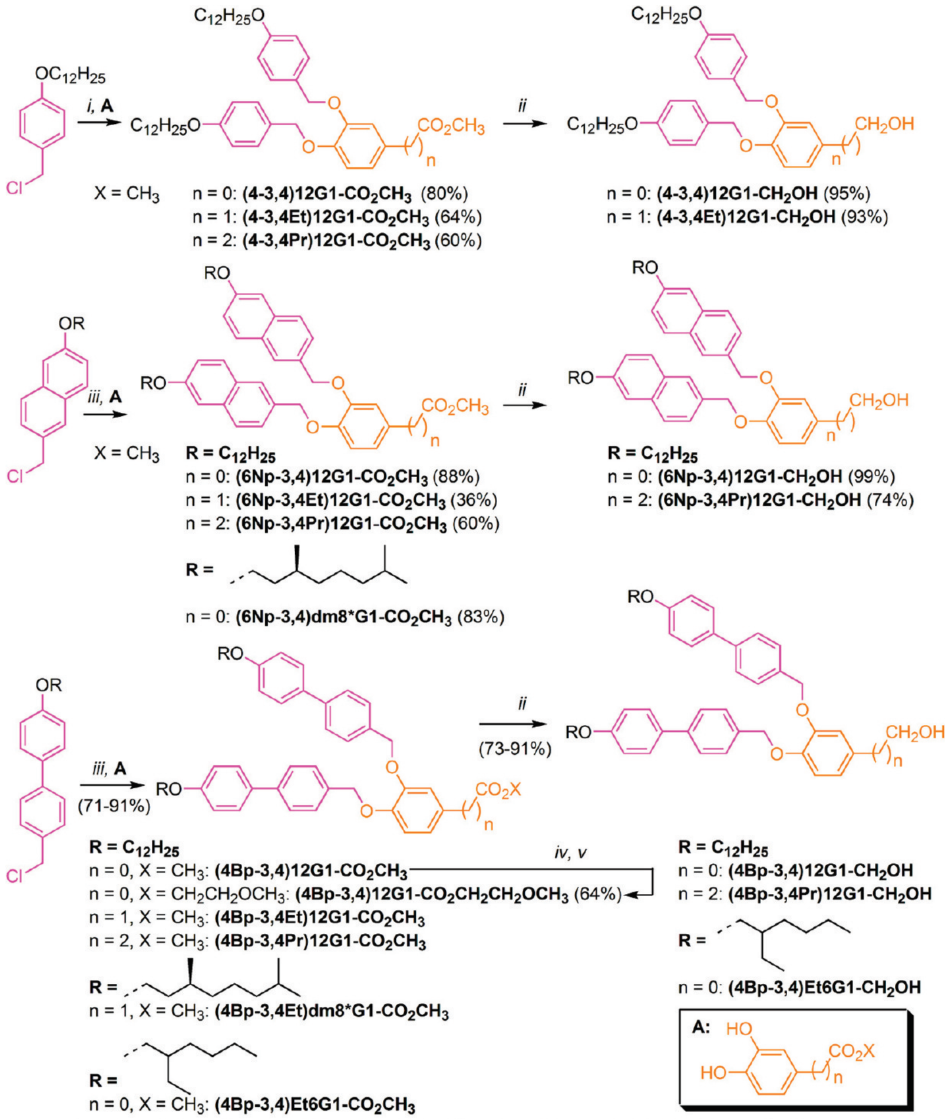

Reagents and Conditions: (i) $K_2CO_3$, DMF, 70°C; (ii) $LiAlH_4$, THF 0 °C - RT; (iii) $K_2CO_3$, DMF, 80-90°C; (iv) KOH, EtOH-THF, 65°C; (v) 2-methoxy ethanol, $PPh_3$, DIAD, THF, RT.

between the primary structure of self-assembling dendrons and their supramolecular structure was expanded to include the doubly segregated columnar and cubic phases. These correlations were also used to elucidate the omnipresent polyhedral shape of the doubly segregated supramolecular assemblies. Structural analysis demonstrates the first example of a hollow dendritic "bulk" vesicle assembled from 1012 dendrons.

## 2. Results and Discussion

**2.1. Synthesis of Hybrid Dendrons.** The three libraries of hybrid dendrons reported in this paper (Schemes 1 and 2) were synthesized according to convergent methods reported previously for the preparation of (4-3,4)12G1-$CO_2CH_3$,[18] (4-3,4)12G1-$CH_2OH$,[18] (6Np-3,4)12G1-$CO_2CH_3$,[9h] and (6Np-3,4)12G1-$CH_2OH$.[9h] Synthesis began with the construction of the benzyl chlorides that will decorate the periphery of the dendrons. (4)12G0-$CH_2Cl$,[19] (6Np)12G0-$CH_2Cl$,[20] and (4Bp)12G0-$CH_2Cl$[20] were prepared according to literature procedures. (6Np)dm8*G0-$CH_2Cl$ was prepared in three steps from methyl 6-hydroxy-2-napthoate (Scheme 1, top).

Alkylation of methyl 6-hydroxy-2-napthoate with (*S*)-1-bromo-2,7-dimethoxyoctane in DMF in the presence of $K_2CO_3$ as a base provided (6Np)dm8*G0-$CO_2CH_3$ in 90% yield. Reduction with $LiAlH_4$ in THF (97% yield) followed by chlorination with $SOCl_2$ in $CH_2Cl_2$ (91% yield) produced (6Np)dm8*G0-$CH_2Cl$. (4Bp)dm8*G0-$CH_2Cl$ and (4Bp)Et6G0-$CH_2Cl$ were prepared similarly to (6Np)dm8*G0-$CH_2Cl$ (Scheme 2, bottom). Methyl 4′-hydroxy-4-biphenylcarboxylate was alkylated with (*S*)-1-bromo-2,7-dimethoxyoctane or 2-ethylhexyl

---

(16) Ungar, G.; Percec, V.; Holerca, M. N.; Johansson, G.; Heck, J. A. *Chem.—Eur. J.* **2000**, *6*, 1258–1266.

(17) Rosen, B. M.; Wilson, D. A.; Wilson, C. J.; Peterca, M.; Won, B. C.; Huang, C.; Lipski, L. R.; Zeng, X.; Ungar, G.; Heiney, P. A.; Percec, V. *J. Am. Chem. Soc.* **2009**, *131*, 17500–17521.

(18) Percec, V.; Cho, W.-D.; Ungar, G. *J. Am. Chem. Soc.* **2000**, *122*, 10273–10281.

(19) Percec, V.; Ahn, C.-H.; Chow, W.-D.; Jamieson, A. M.; Kim, J.; Leman, T.; Schmidt, M.; Gerle, M.; Möller, M.; Prokhorova, S. A.; Sheiko, S. S.; Cheng, S. Z. D.; Zhang, A.; Ungar, G.; Yeardley, D. J. P. *J. Am. Chem. Soc.* **1998**, *120*, 8619–8631.

(20) Percec, V.; Schlueter, D.; Ungar, G.; Cheng, S. Z. D.; Zhang, A. *Macromolecules* **1998**, *31*, 1745–1762.

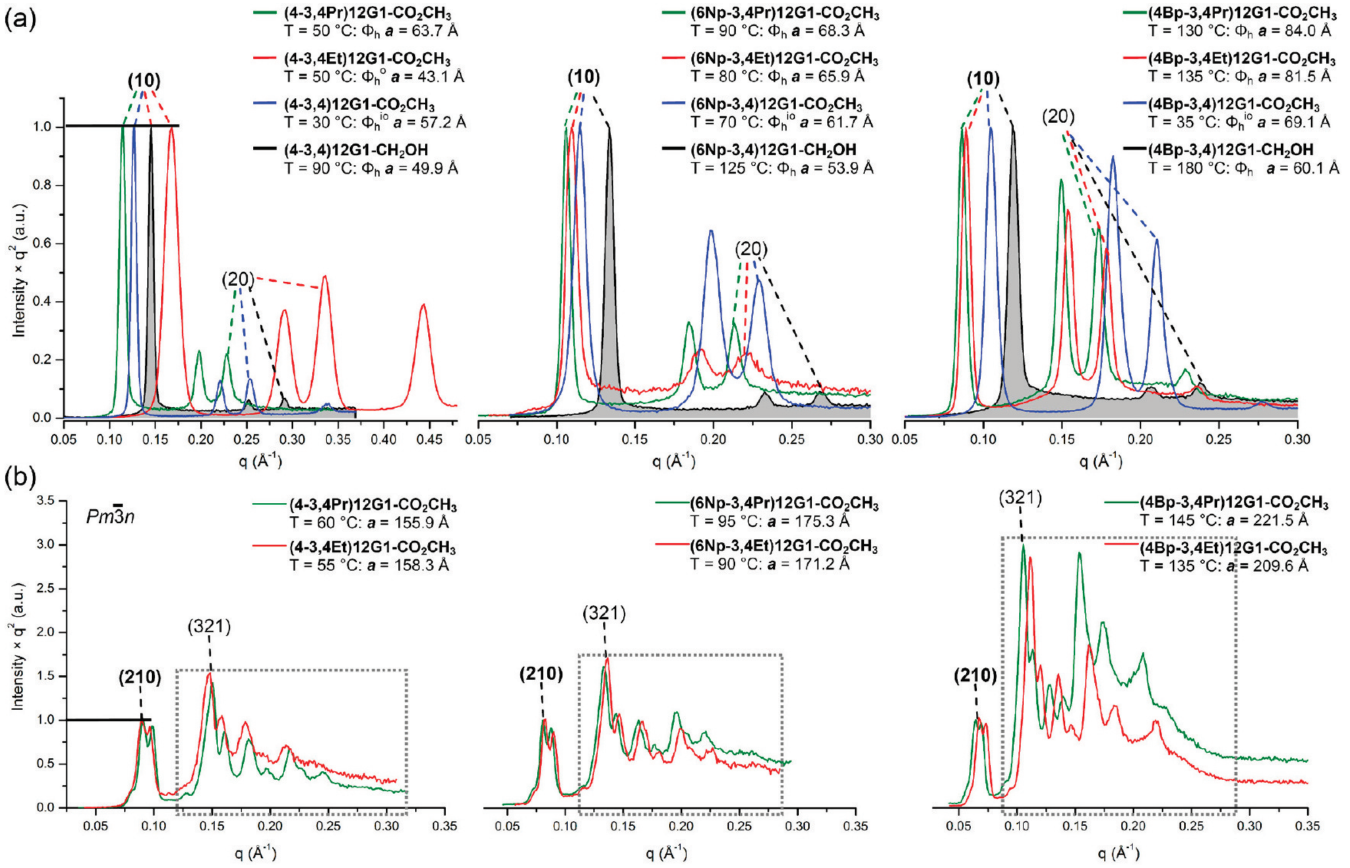

***Figure 1.*** Small-angle powder XRD data collected in the columnar hexagonal (a) and cubic (b) phases self-organized from hybrid dendrons. The data are scaled to the (10) diffraction peak intensity for columnar and to the (210) diffraction peak intensity for cubic phases. The temperature at which the XRD data were recorded, the corresponding phase, and the lattice dimensions are indicated. In (a) the intensity profiles of the dendritic alcohols provide the reference for the increase of the relative intensity of the diffraction peaks with $q_{hk} > q_{10}$ observed for the dendritic esters. In (b) the gray dotted rectangles indicate the diffraction peaks with unusual relative intensity.

bromide in DMF in the presence of $K_2CO_3$ base, giving (4Bp)dm8*G0-$CO_2CH_3$ and (4Bp)Et6G0-$CO_2CH_3$ in 91−95% yield. Reduction with $LiAlH_4$ in THF (88−94% yield), followed by chlorination with $SOCl_2$ in $CH_2Cl_2$ (89−97%), produced (4Bp)dm8*G0-$CH_2Cl$ and (4Bp)Et6G0-$CH_2Cl$.

Achiral and chiral generation one dendrons with esters at the apex were synthesized via the alkylation of nonbranched periphery groups (Scheme 2, purple), (4)12G0-$CH_2Cl$, (6Np)12G0-$CH_2Cl$, (6Np)dm8*12G0-$CH_2Cl$, (4Bp)12G0-$CH_2Cl$, (4Bp)-dm8*12G0-$CH_2Cl$, or (4Bp)Et6G0-$CH_2Cl$, onto branched apex groups (Scheme 2, orange), methyl 3,4-dihydroxybenzoate, methyl 2-(3,4-dihydroxyphenyl)acetate, or methyl 3-(3,4-dihydroxyphenyl)propanoate, in DMF in the presence of $K_2CO_3$ as a base. Reduction of the generation one dendrons with esters at the apex with $LiAlH_4$ in THF produced the corresponding dendritic alcohols. One selected dendritic ester, (4Bp-3,4)12G1-$CO_2CH_3$, was saponified with KOH in hot EtOH−THF to provide (4Bp-3,4)12G1-$CO_2H$ in 92% yield. (4Bp-3,4)12G1-$CO_2CH_2CH_2OCH_3$ was prepared in 70% yield via Mitsunobu esterification of (4Bp-3,4)12G1-$CO_2H$ with 2-methoxyethanol in the presence of diisopropyl azodicarboxylate (DIAD) and $PPh_3$.

**2.2. Structural and Retrostructural Analysis.** Structural analysis, performed via a combination of differential scanning calorimetry, polarized optical microscopy, small- and wide-angle X-ray powder and oriented fiber diffraction experiments, and experimental density measurements,[1a,b,d,g−i,q,s,t] demonstrated that all dendrons self-assemble in supramolecular dendrimers that self-organize into a variety of 2-dimensional or 3-dimensional periodic arrays (Figures 1−3 and Table 1; Figures SF1 and SF2 and Tables ST1 and ST2, Supporting Information). The general trend observed for the dendritic esters is illustrated in Figure 2 and indicates that the addition of one or two methylenic groups to their apexes significantly changes the self-assembly process. For all the benzyl ether, naphthyl methyl ether, and biphenyl methyl ether based dendrons containing an ester group at the apex (Scheme 2), this addition induces the formation of a high-temperature $Pm\bar{3}n$ cubic phase. Furthermore, the hybrid biphenyl methyl ether dendrons exhibit a jump of the diameter of the supramolecular column of their hexagonal phases equal to $a_{hex}$[(4Bp-3,4Pr)12G1-$CO_2CH_3$] − $a_{hex}$[(4Bp-3,4)12G1-$CO_2CH_3$] = 84.0 − 69.1 Å = 14.9 Å. At the same time, the relative intensity of the higher order diffraction peaks of the columnar hexagonal and cubic phases exhibit an unusual enhancement (Figure 1). For example, the relative intensity of the (20) diffraction peak of the hexagonal phase of (4Bp-3,4)12G1-$CH_2OH$ indicated in Figure 1a is area(20)/area(10) = 0.05, whereas for (4Bp-3,4)12G1-$CO_2CH_3$ this ratio increases to area(20)/area(10) = 0.77 (Figure 1a). In the case of the $Pm\bar{3}n$ cubic phases indicated in Figure 1b, the relative intensity of the (321) diffraction peak of (4Bp-3,4Pr)12G1-$CO_2CH_3$ is area(321)/area(210) = 2.4.

Recently,[1s] it was shown that a small enhancement of the higher order diffraction peaks' relative intensity can be generated by the variation of the dendron alkyl chain length. For example, the ratio area(321)/area(210) varied from <0.01 for the dendrons

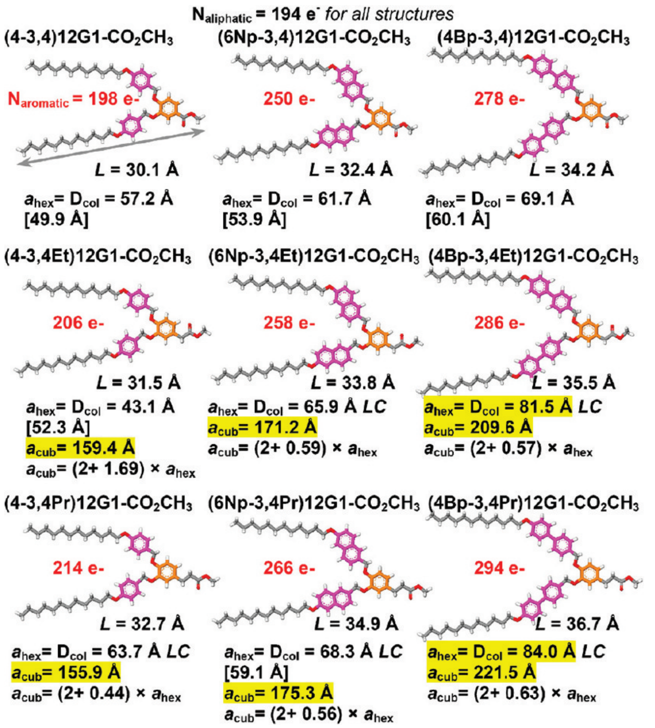

***Figure 2.*** Fully extended molecular models of the first-generation dendrons containing their aliphatic tails in the *all-trans* conformation indicating the maximum possible length of the dendron, *L*. In all cases the column diameters, $D_{col}$, of the hexagonal phases observed from the corresponding dendritic alcohols are given in square brackets. LC = liquid crystal columnar phase. The values marked by a shaded yellow background correspond to a doubly segregated aliphatic−aromatic−aliphatic phase.

containing 14 and 16 C atoms in their alkyl periphery to at most 0.11 for the dendrons containing 6 C atoms in their alkyl periphery.[1s] More significant changes of the powder diffraction intensity profile collected from $Pm\bar{3}n$ cubic phases self-organized from dendritic structures were observed previously upon isomorphous replacement of the apex group and upon the change of the alkyl periphery from hydrogenated to fluorinated chains.[1r] These two examples illustrate a variety of factors that can influence the relative intensity of the higher order diffraction peaks. In the case of supramolecular dendritic hollow structures self-organized into $Pm\bar{3}n$ cubic phases, the ratio area(321)/area(210) was at most 0.8,[7c] which is roughly only one-third of what is observed for the structures shown in Figure 1b. Therefore, the substantial increase in the relative intensity of the higher order diffraction peaks, from 0.11 to 0.8, was previously associated with the presence of a hollow center.[7c,9] As will be shown later, the polyhedral shape of the supramolecular structures self-organized into the bilayer columnar and cubic phases provides an additional factor that contributed to the amplifications illustrated in Figure 1.

In contrast with the majority of dendrons that self-organize in hexagonal and cubic phases, all the structures with 3,4Et and 3,4Pr apexes exhibit an unusual trend: the lattice dimension of the cubic phase is much larger than the expected value, which must be double that of the hexagonal phase[7c] (Table 1, Figure 2). This correlation, $2a_{hex} \approx a_{cub}$, is expected as long as the supramolecular structures preserve their diameter and their internal organization upon the shape change from supramolecular columns to supramolecular spheres. For example, in the case of (4-3,4Et)12G1-CO$_2$CH$_3$ and (4Bp-3,4Pr)12G1-CO$_2$CH$_3$ dendritic esters the expected[7c] lattice parameters of the cubic phases, $2a_{hex}$, are 86.2 and 168.0 Å, respectively. The experimental values of $a_{cub}$ = 159.4 and 221.5 Å are, respectively, 85% and 32% larger than the expected dimensions. This observation coupled with the significant enhancement of the higher order diffraction peaks observed for both cubic and hexagonal phases (Figure 1) is the first indication that these structures follow different self-assembly routes upon the first-order transition from hexagonal to cubic phases.

The second result that suggests a different pathway of the self-assembly process is extracted from the analysis of the wide-angle X-ray scattering (WAXS) patterns collected from oriented fibers[1q] in the columnar hexagonal phase. Figure 3 shows that the larger-than-expected hexagonal phases, observed for the

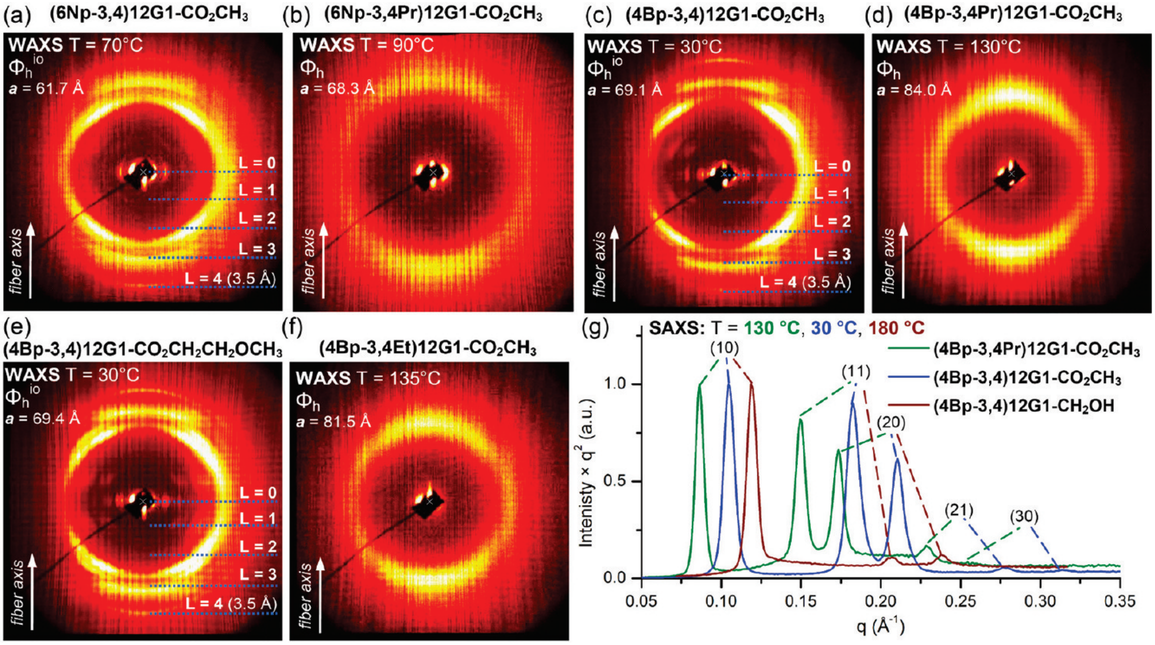

***Figure 3.*** WAXS patterns collected from the oriented fibers of the indicated hybrid dendrons (a−f). Small-angle powder XRD data for the compounds from (c) and (d) and of the hybrid dendritic alcohol (4Bp-3,4)12G1-CH$_2$OH at corresponding temperatures (g).

***Table 1.*** Structural and Retrostructural Analysis of the Libraries of First-Generation Hybrid Dendrons

| compd | $T$ (°C) | phase[a] | shape of the supramolecular structure[b] | $a$, $b$[c] (Å) | $d_{10}$, $d_{11}$, $d_{20}$, $d_{21}$, $d_{30}$ (Å);[d]<br>$d_{001}$, $d_{002}$, $d_{003}$, $d_{004}$ (Å);[e]<br>$d_{200}$, $d_{210}$, $d_{211}$, $d_{321}$, $d_{400}$, $d_{420}$ (Å);[f]<br>$d_{20}$, $d_{11}$, $d_{31}$, $d_{40}$, $d_{02}$, $d_{22}$ (Å)[g] | $M$[h] | $t$[i] (Å) | $\rho$[j] (g/cm$^3$) | $\mu$[k] | $\mu_c$[l] | $\gamma$[m] (deg) |
|---|---|---|---|---|---|---|---|---|---|---|---|
| (4-3,4)12G1-$CO_2CH_3$ | 30 | $\Phi_h^{io}$ | | 57.2 | 49.6, 28.6, 24.8, 18.7 | 717 | 3.5 | 1.0[p] | 8 | | |
| | 56 | $\Phi_h$ | | 57.4 | 49.8, 28.7, 24.9, 18.8 | | | | | | |
| (4-3,4Et)12G1-$CO_2CH_3$ | 20 | $L_k$[n] | | 45.7 | 45.7, 22.8 | 731 | | 1.0[p] | | | |
| | 55 | $Pm\bar{3}n$ | Polyh-B | 159.4 | 79.9, 71.5, 65.2, 42.7, 39.9, 35.7 | | | | 442 | 19 | |
| | 45 | $\Phi_{r\text{-}c}$ | | 132.1, 52.2 | 66.1, 48.6, 33.7, 33.0, 26.1, 24.3 | | | | | | 68.4 |
| | −10 | $L_k$[o] | | 56.0 | 56.1, 28.0, 18.7 | | | | | | |
| | −10 | $\Phi_h^o$[q] | Polyh | 42.2 | 36.6, 21.1, 18.3 | | | | | | |
| | 50 | $\Phi_h^o$ | Polyh | 43.1 | 37.4, 21.6, 18.7, 14.1 | | 4.5 | | 6 | | |
| (4-3,4Pr)12G1-$CO_2CH_3$ | 30 | $L_k$[n] | | 50.3 | 50.3, 25.2 | 745 | | 1.0[p] | | | |
| | 60 | $Pm\bar{3}n$ | Polyh-B | 155.9 | 77.9, 69.7, 63.7, 41.7, 38.9, 34.9 | | | | 382 | 17 | |
| | 50 | $\Phi_h$ | | 63.7 | 55.2, 31.9, 27.6 | | 4.5 | | 12 | | |
| | 30 | $\Phi_{r\text{-}c}$ | | 124.8, 57.2 | 62.6, 52.2, 33.7, 31.2, 28.6, 26.0 | | | | | | 65.4 |
| | −6 | $L_k$ | | 57.4 | 57.4, 28.7, 19.1, 14.3 | | | | | | |
| | 45 | L | | 50.2 | 50.2, 25.1 | | | | | | |
| (6Np-3,4)12G1-$CO_2CH_3$ | 25 | $L_k$[n] | | 55.4 | 55.4, 27.7, 18.5 | 817 | | 1.08 | | | |
| | 70 | $\Phi_h^{io}$ | Polyh-H | 61.7 | 53.6, 30.8, 26.7 | | 3.5 | | 8 | | |
| (6Np-3,4)dm8*G1-$CO_2CH_3$ | 100 | $\Phi_h^o$ | Polyh-B | 66.7 | 58.0, 33.5, 28.9, 21.9 | 761 | 3.5 | 1.08[p] | 12 | | |
| (6Np-3,4Et)12G1-$CO_2CH_3$ | 30 | L | | 56.6 | 56.6, 28.3, 18.9 | 831 | | 1.08[p] | | | |
| | 80 | $\Phi_h$ | Polyh-B | 65.9 | 57.2, 32.9, 28.6 | | 4.5 | | 13 | | |
| | 90 | $Pm\bar{3}n$ | Polyh-B | 171.2 | 85.6, 76.6, 69.9, 45.8, 42.8, 38.3 | | | | 490 | 20 | |
| | 70 | $\Phi_{r\text{-}c}$ | | 136.2, 55.4 | 68.2, 51.8, 35.2, 34.1, 27.7, 25.7 | | | | | | 67.9 |
| | −20 | $L_k$ | | 56.4 | 56.4, 28.2, 18.8 | | | | | | |
| (6Np-3,4Pr)12G1-$CO_2CH_3$ | 30 | $L_k$ | | 58.2 | 58.2, 29.1, 19.4 | 845 | | 1.08[p] | | | |
| | 60 | L | | 50.3 | 50.3, 25.2 | | | | | | |
| | 90 | $\Phi_h$ | Polyh-B | 68.3 | 59.4, 34.1, 29.5 | | 4.5 | | 14 | | |
| | 95 | $Pm\bar{3}n$ | Polyh-B | 175.3 | 87.6, 78.4, 71.6, 48.6, 43.8, 39.2 | | | | 518 | 21 | |
| (4Bp-3,4)12G1-$CO_2CH_3$ | 35 | $\Phi_h^{io}$ | Polyh-H | 69.1 | 59.9, 34.5, 29.9, 22.6, 19.9 | 869 | 3.5 | 1.08 | 10 | | |
| | 150 | $\Phi_x$ | | | 36.9 | | | | | | |
| (4Bp-3,4Et)12G1-$CO_2CH_3$ | 30 | $L_k$ | | 60.6 | 60.6, 30.3, 20.2 | 883 | | 1.115 | | | |
| | 115 | $\Phi_{r\text{-}c}$ | | 167.8, 58.3 | 84.5, 55.2, 40.2, 42.2, 29.2, 27.5 | | | | | | 70.8 |
| | 135 | $\Phi_h$ | Polyh-B | 81.5 | 70.8, 40.8, 35.3, 26.6 | | 4.6 | | 20 | | |
| | 145 | $Pm\bar{3}n$ | Polyh-B | 209.6 | 104.8, 93.7, 85.6, 56.0, 52.4, 46.9 | | | | 876 | 30 | |
| (4Bp-3,4Et)dm8*G1-$CO_2CH_3$ | 5 | $\Phi_{r\text{-}c}^o$ | | 104.3, 50.4 | 52.4, 45.4, 28.6, 26.1, 25.2, 22.7 | 827 | | 1.08[p] | | | 64.2 |
| | 90 | $L_k$ | | 44.7 | 44.7, 22.3 | | | | | | |
| | 130 | $Pm\bar{3}n$ | Polyh-B | 173.8 | 86.9, 77.7, 70.9, 46.4, 43.4, 38.9 | | 4.6 | | 516 | 22 | |
| (4Bp-3,4Pr)12G1-$CO_2CH_3$ | 25 | $L_k$ | | 63.2 | 63.2, 31.6, 21.1, 15.8 | 897 | | 1.109 | | | |
| | 110 | $\Phi_{r\text{-}c}$ | | 170.8, 62.4 | 85.9, 58.7, 41.9, 42.7, 31.1, 29.3 | | | | | | 69.9 |
| | 130 | $\Phi_h$ | Polyh-B | 84.0 | 72.9, 41.9, 36.3, 27.5 | | 4.6 | | 21 | | |
| | 145 | $Pm\bar{3}n$ | Polyh-BH | 221.5 | 110.7, 99.1, 90.4, 59.2, 55.4, 49.5 | | | | 1012 | 33 | |
| (4Bp-3,4)12G1-$CO_2CH_2CH_2OCH_3$ | 25 | $\Phi_h^{io}$ | Polyh-H | 69.4 | 60.2, 34.7, 30.1, 23.2, 20.0 | 913 | 3.5 | 1.1[p] | 10 | | |
| | 125 | $\Phi_{r\text{-}c}$ | | 159.0, 63.7 | 79.7, 59.2, 40.8, 39.7, 31.9, 29.6 | | | | | | 68.2 |
| | 150 | $\Phi_x$ | | | 36.8 | | | | | | |
| (4Bp-3,4)Et6G1-$CO_2CH_3$ | 30 | $\Phi_{r\text{-}c}^o$ | Polyh | 79.8, 58.2 | 39.9, 47.2, 24.2, 19.9, 29.1, 23.5 | 757 | | 1.1[p] | | | 53.9 |
| | 125 | $Pm\bar{3}n$ | Polyh-B | 139.2 | 69.8, 62.2, 56.7, 37.2, 34.8, 31.1 | | | | 298 | 16 | |
| | 95 | $\Phi_h$ | Polyh | 56.1 | 48.7, 28.0, 24.3 | | 4.6 | | 11 | | |

---

[a] Phase notation: $\Phi_h$, columnar hexagonal phase; $\Phi_{r\text{-}c}$, centered rectangular columnar phase; $Pm\bar{3}n$, cubic phase; L, lamellar phase; $L_k$, ordered lamellar phase; $\Phi_h^o$, ordered columnar hexagonal phase; $\Phi_{r\text{-}c}^o$, ordered centered rectangular columnar phase; $\Phi_x$, unidentified columnar phase; $\Phi_h^{io}$, columnar hexagonal phase with intracolumnar order. [b] Shape and internal structure of the supramolecular structure: Polyh, singly segregated polyhedral cluster; Polyh-H, hollow singly segregated polyhedral structure; Polyh-B, doubly segregated polyhedral structure; Polyh-BH, hollow doubly segregated polyhedral structure. [c] Lattice parameters calculated using $a = (2/\sqrt{3})(d_{10} + (\sqrt{3})d_{11} + 2d_{20} + (\sqrt{7})d_{21})/4$ for hexagonal phases, $a = (d_{001} + 2d_{002})/2$ for lamellar phases, $a = (2d_{200} + (\sqrt{5})d_{210} + (\sqrt{6})d_{211})/3$ for $Pm\bar{3}n$ cubic phases, and $a = (2d_{20} + 4d_{40})/2$ and $b = 2d_{02}$ for centered rectangular columnar phases. [d] $d$-spacing for columnar hexagonal phases. [e] $d$-spacing for lamellar phases. [f] $d$-spacing for $Pm\bar{3}n$ cubic phases. [g] $d$-spacing for centered rectangular columnar phases. [h] Molecular weight. [i] Average column stratum thickness calculated within a range of ±0.2 Å from the WAXS patterns. [j] Experimental density at 20 °C. [k] Number of dendrons per supramolecular column stratum or cluster calculated using $\mu = (a^2t(\sqrt{3})/2)\rho N_A/M$ for hexagonal phases and $\mu = (a^3/8)\rho N_A/M$ for $Pm\bar{3}n$ cubic phases, where $N_A = 6.022 \times 10^{23}$ mol$^{-1}$ = Avogadro's number. [l] Number of dendrons in the cross-section of the supramolecular clusters of the $Pm\bar{3}n$ cubic phase calculated using $\mu = (\pi a^2 t/16)\rho N_A/M$. [m] Angle defined by $\gamma = \angle(\vec{a}+\vec{b}, \vec{b})$ and calculated using $\gamma = \tan^{-1}(a/b)$. [n] Phase observed only in the first heating cycle of the as-prepared compound. [o] Phase observed only in the cooling cycle at 10 °C/min. [p] Density values were assumed to be 1.0 g/cm$^3$ for the benzyl ether library. For the naphtyl methyl ether and biphenyl methyl ether libraries, the experimental values available for selected structures were assumed for the other structure of the corresponding library. [q] Phase observed only in the cooling cycle at 1 °C/min.

hybrid biphenyl methyl ether dendritic esters, are liquid crystals. Therefore, the enhancement of the higher order diffraction peaks of the columnar hexagonal phases (Figures 1 and 3g) was not generated by intracolumnar correlations. Such an effect, related to possible dendron tilt correlations, has been observed in the self-assembly of (4-3,4Et)12G1-$CO_2CH_3$ and will be discussed in an another subsection. Assuming that in the observed $Pm\bar{3}n$ cubic phases the self-assembly process follows the "traditional" single aliphatic-to-aromatic microphase segregation,[1a,r,s] from molecular modeling and experimental lattice parameters we find that the supramolecular structures must have unusually large empty domains (Supporting Information, Figure SF4). The diameters of the empty regions are large enough to accommodate at least one dendron with dimensions corresponding to the fully

***Scheme 3.*** Schematic Representation of the Self-Assembly of Dendrons into Bilayer Structures

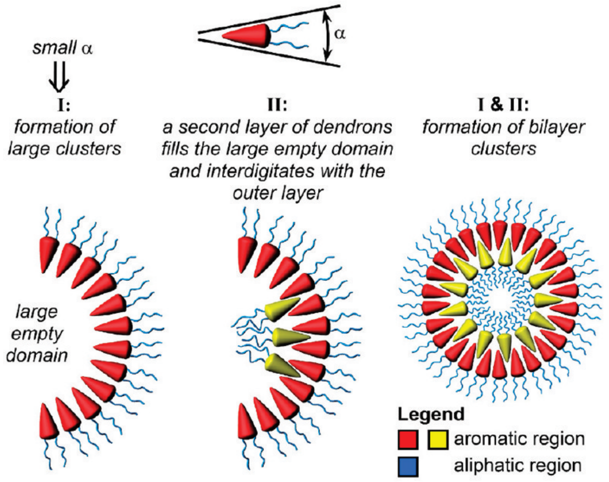

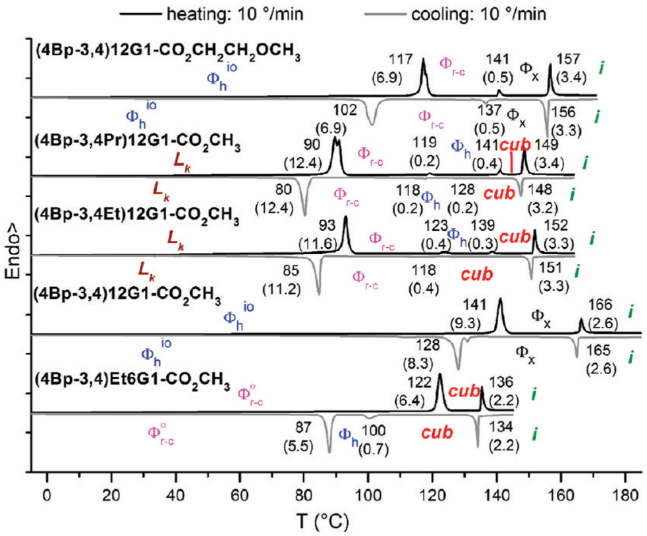

***Figure 4.*** Second heating (black lines) and cooling (gray lines) differential scanning calorimetry traces (both recorded at 10 °C/min) collected from biphenyl methyl ether hybrid dendrons. The compound, phases, transition temperatures (°C), and associated enthalpy changes (in parentheses, kcal/mol) are indicated.

extended *all-trans* conformation shown in Figure 2. The self-assembly process of the first-generation hybrid dendritic esters is driven by weak interactions. In the absence of stronger interactions, such as H-bonding[7c,9] or ionic, the noncovalent interactions are not strong enough to sustain a very large hollow core. As will be shown later, this hollow region confers a significant penalty to the free energy of the system. Therefore, the most probable model supported by electron density reconstructions, powder X-ray diffraction simulations, experimental lattice parameters, and molecular modeling consists of the doubly segregated aliphatic−aromatic supramolecular structure illustrated in Scheme 3. This model fills completely or reduces the diameter of the large hollow cavity shown in Figure SF4 and Scheme 3.

To understand the mechanism for the formation of doubly segregated clusters, we imagine splitting the self-assembly process into two stages. The addition of one or two methylenic units to the carboxylate group from the apex of the dendron reduces its solid angle.[16] In the first stage, these “sharp” dendrons are expected to self-assemble into large structures with small curvature, which in turn forms the outer layer (Scheme 3). In the second stage, because the outer layer has an unusually large diameter, the system can further minimize the free energy by filling the empty region with a second layer of dendrons. For clarity, the inner layer is shown in Scheme 3 with the aromatic region colored in yellow. If we combine these two stages, we form an outer layer with small curvature and an inner layer that interdigitates with the outer larger one to further maximize the layer-to-layer interactions. This mechanism, illustrated in Scheme 3, does not contradict the segregation of the aliphatic and aromatic regions. At the same time, the proposed interdigitated mechanism is supported by the fact that none of the dendritic alcohols investigated so far self-assemble into an interdigitated cubic or bilayer hexagonal phase (Tables ST1 and ST2, Supporting Information). In these structures, the addition of strong apex-to-apex H-bonding interactions, for example, via apex alcohol groups, prohibits the formation of the interdigitated packing of the bilayer aromatic region. Similarly, potential bilayer cubic phases were identified in the previously published higher generation dendritic esters (4Bp-3,4Bp-3,5Bp)12G2-$CO_2CH_3$[1h] and (4BpPr-3,4BpPr-3,5BpPr)-12G2-$CO_2CH_3$.[17] By contrast, no cubic phase was observed in the corresponding dendritic alcohols.[1h,17] In addition, the large variation of the correlation between the lattice parameters, $a_{\text{cub}} = (2 + x)a_{\text{hex}}$, with $x$ ranging from 0.44 to 1.69 (Figure 2), can be explained by the alternative pathways of self-assembly at the transition from either singly or doubly segregated columns to doubly segregated vesicles.

The mechanism shown in Scheme 3 resembles the assembly of biological vesicles in dilute solutions.[8,13] In the case of the dendritic vesicles, the aliphatic−aromatic segregation replaces the biological vesicle hydrophobic−hydrophilic segregation. Nevertheless, the underlying mechanism that generates the two segregations is completely different. In biological vesicles the interaction with water generates the hydrophobic−hydrophilic segregation and their formation, whereas in the dendritic vesicles the double segregation is mediated by the dendron−dendron interactions (Scheme 3).

**2.3. Analysis of the Hexagonal Phases Self-Organized from Polyhedral Supramolecular Columns.** A closer inspection of the intensity profiles of the small-angle X-ray powder diffraction data summarized in Figure 1, and of the DSC traces for selected biphenyl methyl ether dendritic esters shown in Figure 4, reveals the complexity of the self-assembly and self-organization process. The intensity profiles of the cubic phases reported in Figure 1b exhibit a gradual increase of the relative intensity of the higher order diffraction peaks. This enhancement follows the increase of the lattice dimension, as well as the change of the aromatic structure from benzyl ether to naphthyl methyl ether and to biphenyl methyl ether. The most significant change is observed in the biphenyl methyl ether case. With the exception of (4-3,4Et)12G1-$CO_2CH_3$, the intensity profiles of the XRD data collected in the columnar hexagonal phases shown in Figure 1a follow a similar trend. The largest increase is again observed upon the change from naphthyl methyl ether to biphenyl methyl ether based dendrons with 3,4Et and 3,4Pr groups at their apexes.

**2.3.1. Powder X-ray Diffraction Phase Problem for Hollow and Nonhollow Polyhedral Columns.** We have suggested that the formation of the supramolecular assemblies self-organized in the observed cubic phases must follow a doubly segregated self-assembly process. Janus dendrimers, functionalized with perfluorinated chains on one side and hydrogenated chains on the other, were reported to self-assemble into supramolecular bilayer columns.[21] In these structures, the self-assembly process into bilayer columns followed a perfluorinated aromatic−aliphatic segregation. Molecular modeling combined with the analysis of the lattice dimensions of the columnar hexagonal phases (Supporting Information, Figure SF4) suggested that the (4Bp-3,4)12G1-CO$_2$CH$_3$ and (4Bp-3,4Pr)12G1-CO$_2$CH$_3$ hybrid dendrons may have empty core diameters, $D_{\text{core}}$, of at least 14 and 27 Å, respectively. Previously,[7c,9] enhanced higher order diffraction peaks were associated with the presence of hollow centers, but as will be shown later in this section, for the structures investigated here the interpretation of the XRD intensity profiles is more complex. Inspired by the observation that the high-temperature phase of (4Bp-3,4Pr)12G1-CO$_2$CH$_3$ is a bilayer vesicular cubic structure, we decided to discriminate between low-temperature hexagonal phases formed by hollow and bilayer columns. The difficulty of distinguishing between these two models arises from the complexity of assessing which reconstructed electron density map corresponds to the physical structure. A powder X-ray diffraction experiment yields the integrated intensities of the diffraction peaks. These intensities are proportional to the square of the structure factors. Thus, the square root of the measured intensity, which after the appropriate multiplicity correction we will refer to as the “amplitude”, allows us to determine the relative magnitudes of the structure factors, but not their phases. Lattice centrosymmetry reduces the complexity of the “phase problem” for the investigated hexagonal, centered rectangular, and $Pm\bar{3}n$ cubic phases. In general, phase values can range from 0 to $\pi$. However, for these centrosymmetric lattices the phase values are restricted to being either 0 or $\pi$.

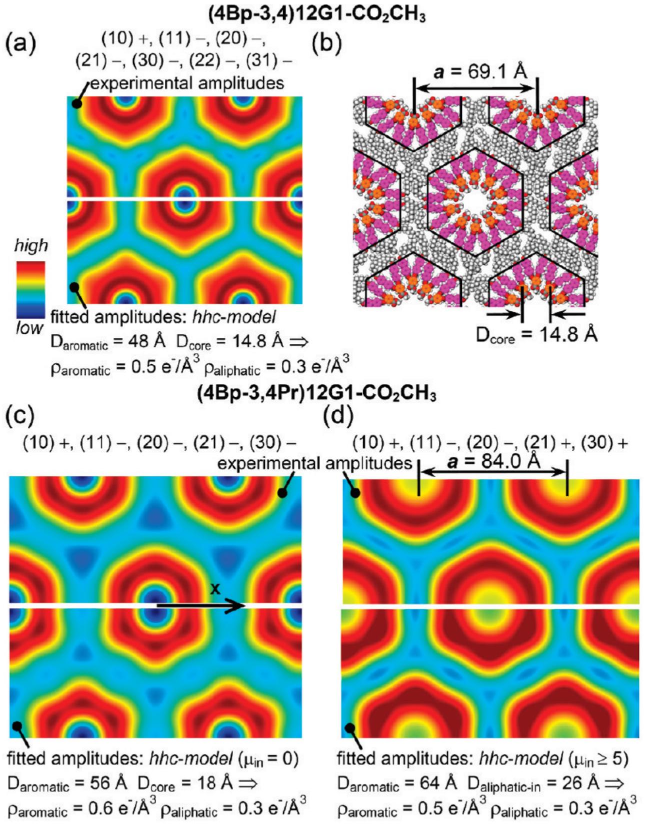

***Figure 5.*** Reconstructed relative electron density maps of the columnar hexagonal phase self-organized from (4Bp-3,4)12G1-CO$_2$CH$_3$ (a), (4Bp-3,4Pr)12G1-CO$_2$CH$_3$ (c, d), and (4Bp-3,4)12G1-CO$_2$CH$_3$ molecular models based on the fitted parameters shown at scale with the corresponding electron density maps (b). In all cases the diffraction peak phase + or − is indicated. The parameters $D_{\text{aromatic}}$, $D_{\text{core}}$, and $D_{\text{aliphatic-in}}$, extracted from the fits of the experimental powder XRD data using the hhc models, provided the absolute electron densities of the aromatic ($\rho_{\text{aromatic}}$) and aliphatic ($\rho_{\text{aliphatic}}$) regions that were used to support the phase solutions proposed in (a) and (d) and to eliminate the solution shown in (c).

Figure 5 illustrates the relative electron density distributions of the columnar hexagonal phases self-organized from (4Bp-3,4)12G1-CO$_2$CH$_3$ and (4Bp-3,4Pr)12G1-CO$_2$CH$_3$, reconstructed from the intensities calculated from their powder X-ray data shown in Figure 3g. From all the possible combinations of phases, + or −, the solutions selected in Figure 5 followed the general principle used to generate electron density maps that exhibit a microsegregation of the aromatic and aliphatic regions.[7d,c,9] The significant relative intensity of the (11) and (20) diffraction peaks, shown in Figure 3g, dominates the other terms included in the reconstruction of the Fourier series of the electron density maps. Therefore, independent of the amplitude phase choice of the other higher order diffraction peaks, (21), (30), (22), and (31), all the electron density maps exhibit a polygonal-shaped aromatic distribution for the case of (10)+, (11)−, and (20)−. Any other phase combination for these three amplitudes did not generate the expected microsegregation of the aromatic and aliphatic regions, and they were eliminated. From the possible phase combination of the other diffraction peaks, (21), (30), (22), and (31), for (4Bp-3,4)12G1-CO$_2$CH$_3$ one solution is shown in Figure 5a and for (4Bp-3,4Pr)12G1-CO$_2$CH$_3$ there are two possible solutions shown in Figure 5c,d. In addition, Figure 5 illustrates the excellent agreement of the electron density distribution reconstructed from the experimental amplitudes and from the hhc model fitted amplitudes, using the analytical methodology that will be elaborated on in the next subchapter.

Molecular models of the columnar hexagonal phase and their reconstructed electron density distribution shown in Figure 5a,b demonstrate that (4Bp-3,4)12G1-CO$_2$CH$_3$ self-assembles into singly segregated hollow polyhedral columns with the diameter of the hollow region $D_{\text{core}} = 14.8 \pm 3.5$ Å. Assuming that the columns of the hexagonal phase assembled from (4Bp-3,4Pr)12G1-CO$_2$CH$_3$ are also singly segregated, the molecular model provided a lower bound of the diameter of the hollow region of 27 Å (Supporting Information, Figure SF4). For the hybrid (4Bp-3,4)12G1-CO$_2$CH$_3$ the hollow region corresponds to a relatively small volume fraction that represents $(D_{\text{core}} \approx 14.8\ \text{Å}/D_{\text{col}} = 69.1\ \text{Å})^2 \approx 4.5\%$ of all the supramolecular columns. On the other hand, for (4Bp-3,4Pr)12G1-CO$_2$CH$_3$ the volume fraction of the hypothetical hollow region is more than 2 times larger $(D_{\text{core}} \approx 27\ \text{Å}/D_{\text{col}} = 84\ \text{Å})^2 \approx 10.3\%$. Assuming that the addition of one or two methylenic units at the apex of the dendron does not significantly strengthen dendron−dendron interactions, it is unrealistic to observe such a large increase of the hollow region since it would impart a significant free energy penalty. To prove that the phase solution (+, −, −, −, −) shown in Figure 5c does not correspond to a hollow singly segregated column, we compare the diameter of the hollow center of 18 Å, provided by the simulation, with the 27 Å value calculated from molecular model. The 27 Å value is 50% larger than the 18 Å fitted value, and therefore, the phase solution (+, −, −, −, −) does not correspond to a hollow singly segregated column. Therefore, we conclude that the columnar hexagonal phase of (4Bp-3,4Pr)12G1-CO$_2$CH$_3$ is generated by supramo-

---

(21) Percec, V.; Imam, M. R.; Bera, T. K.; Balagurusamy, V. S. K.; Peterca, M.; Heiney, P. A. *Angew. Chem., Int. Ed.* **2005**, *44*, 4739–4745.

***Table 2.*** Calculation of the Number of Dendrons Forming the Inner Layer, $\mu_{in}$, and Outer Layer, $\mu_{out}$, of the Hybrid Dendritic Esters Self-Assembled into Doubly Segregated Aliphatic−Aromatic Structures

| compd | phase[a] | $a/2^b$ (Å), $a/4^c$ (Å) | $\mu^d$ | $\lambda$, $\delta^e$(Å) | $\alpha^f$ (deg) | $\alpha'^g$ (deg) | $\mu_{in\text{-}A}{}^h$ | $\mu_{out\text{-}A}{}^i$ | $\mu_{in\text{-}u}{}^j$ | $r^k$(Å) | $\mu_{in\text{-}B}{}^l$ | $\mu_{out\text{-}B}{}^m$ |
|---|---|---|---|---|---|---|---|---|---|---|---|---|
| (4Bp-3,4Pr)12G1-$CO_2CH_3$ | $\Phi_h$ | 42.0 | 21 | 29, 14 | 24.61 | 35.96 | 6.4 | 14.6 | 3.50 | 2.24 | 4.5 | 16.5 |
| | $Pm\bar{3}n$ | 55.4 | 33 | 29, 14 | 20.52 | 39.78 | 15.5 | 17.5 | 4.17 | 2.56 | 5.6 | 27.4 |
| (4Bp-3,4Et)12G1-$CO_2CH_3$ | $\Phi_h$ | 40.8 | 20 | 27.8, 14 | 26.11 | 38.68 | 6.2 | 13.8 | 3.43 | 2.21 | 4.3 | 15.7 |
| | $Pm\bar{3}n$ | 52.4 | 30 | 27.8, 14 | 22.24 | 42.63 | 13.8 | 16.2 | 4.01 | 2.48 | 5.3 | 24.7 |
| (6 Np-3,4Pr)12G1-$CO_2CH_3$ | $\Phi_h{}^{n}$ | 34.2 | 14 | 27.2, 14 | 32.08 | 40.65 | 2.8 | 11.2 | 2.87 | 1.97 | 3.5 | 10.5 |
| | $Pm\bar{3}n$ | 43.8 | 21 | 27.2, 14 | 27.19 | 44.51 | 7.8 | 13.2 | 3.36 | 2.17 | 4.3 | 16.7 |
| (6 Np-3,4Et)12G1-$CO_2CH_3$ | $\Phi_h{}^{n}$ | 33.0 | 13 | 26.1, 14 | 34.68 | 44.27 | 2.6 | 10.4 | 2.76 | 1.93 | 3.4 | 9.6 |
| | $Pm\bar{3}n$ | 42.8 | 20 | 26.1, 14 | 28.95 | 48.40 | 7.6 | 12.4 | 3.27 | 2.14 | 4.1 | 15.9 |
| (4-3,4Pr)12G1-$CO_2CH_3$ | $\Phi_h{}^{n}$ | 31.9 | 12 | 25, 14 | 37.76 | 48.69 | 2.5 | 9.5 | 2.63 | 1.88 | 3.2 | 8.8 |
| | $Pm\bar{3}n$ | 39.0 | 17 | 25, 14 | 32.34 | 51.47 | 5.9 | 11.1 | 3.05 | 2.04 | 3.8 | 13.2 |
| (4−3,4Et)12G1-$CO_2CH_3$ | $Pm\bar{3}n$ | 39.9 | 19 | 23.8, 14 | 30.98 | 53.12 | 7.4 | 11.6 | 3.33 | 2.16 | 4.2 | 14.8 |
| (4Bp-3,4Et)dm8*G1-$CO_2CH_3$ | $Pm\bar{3}n$ | 43.5 | 22 | 25, 11 | 27.84 | 49.43 | 9.1 | 12.9 | 2.78 | 1.94 | 3.7 | 18.3 |
| (4Bp-3,4)Et6G1-$CO_2CH_3$ | $Pm\bar{3}n$ | 34.8 | 16 | 23, 9 | 33.38 | 51.51 | 4.8 | 11.2 | 2.07 | 1.75 | 2.8 | 13.2 |
| (6 Np-3,4)dm8*G1-$CO_2CH_3$ | $\Phi_h{}^{o}$ | 33.4 | 12 | 24, 11 | 40.84 | 58.10 | 3.2 | 8.8 | 1.98 | 1.75 | 2.5 | 9.5 |

[a] Lattice notation: $\Phi_h$, columnar hexagonal; $\Phi_h{}^{o}$, ordered columnar hexagonal; $Pm\bar{3}n$, cubic. [b] Radius of the supramolecular assembly calculated for the columnar hexagonal phases from $a/2$, where $a$ is the lattice dimension listed in Table 1. [c] Radius of the supramolecular assembly calculated for the cubic phases from $a/4$, where $a$ is the lattice dimension listed in Table 1. [d] Number of dendrons per assembly cross-section as calculated in Table 1. [e] The dendron length, $\lambda$, used in method A and average aliphatic region thickness, $\delta$, used in method B were calculated from the molecular models with mixed trans−gauche conformation for the alkyl chains shown in Figure SF4 (Supporting Information), assuming no assembly-to-assembly interdigitation. [f] Angles defined in Figure 6 were calculated using method A from eqs SE3 and SE4 (Supporting Information):$\alpha = 2\sin^{-1}[\lambda(a/2)\sin(\alpha'/2)]$. [g] Angles defined in Figure 6 were calculated using method A from eqs SE3 and SE4 (Supporting Information): $\alpha' = \pi(a/2)^2/(\lambda^2\mu/2)$. [h] Number of dendrons forming the inner layer, calculated using method A from eq SE2 (Supporting Information): $\mu_{in\text{-}A} = \mu - \mu_{out\text{-}A}$. [i] Number of dendrons forming the outer layer, calculated using method A from eq SE2 (Supporting Information): $\mu_{out\text{-}A} = 360°/\alpha$. [j] Number of dendrons (uncorrected, first iteration of the nonlinear system of eqs SE5 and SE6 (Supporting Information)) forming the inner layer calculated using method B with $r = 0$ in eq SE5: $\mu_{in\text{-}u} = \mu/(a/\delta)$. [k] Correction factor $r$ calculated from $r = (3.5\ Å/2)/\sin[360°/(2\ \mu_{in\text{-}u})]$ as shown in Figure 6b. [l] Number of dendrons forming the inner layer, calculated using method B with nonzero correction factor $r$ in eq SE5 (Supporting Information): $\mu_{in\text{-}B} = \mu/[1 + (a\delta - \delta^2)/(\delta - r)^2]$. [m] Number of dendrons forming the outer layer, calculated using method B with nonzero correction factor $r$ in eq SE5 (Supporting Information): $\mu_{out\text{-}B} = \mu - \mu_{in\text{-}B}$. [n] The bilayer assignment is not definitive; these hexagonal phases have relatively small $D_{col}$.

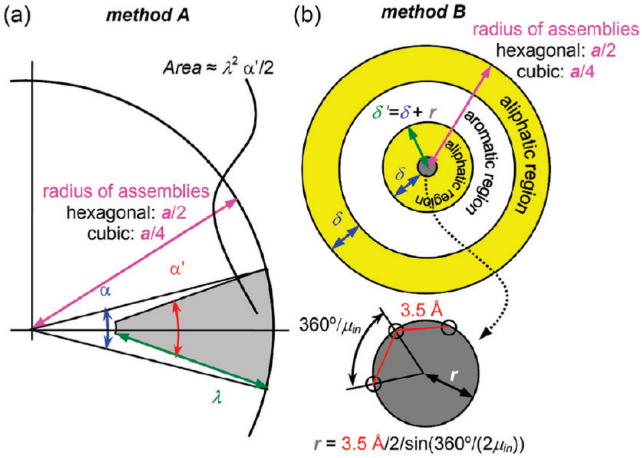

***Figure 6.*** Simplified models of the supramolecular assemblies forming the hexagonal and cubic bilayer phases used to calculate the projection of the solid angle of the dendron, α′, by method A (a) and of the close contact correction factor, $r$, by method B (b). For clarity in (a) only one dendron from the outer layer of the bilayer assembly is shown. $a$ = lattice parameter, $\lambda$ = length of the dendron, α and α′ are the two indicated angles, $\delta$ = aliphatic region thickness, and $r$ = close contact correction factor. Complete details of the calculations are given in section 5.3 of the Supporting Information.

lecular columns that are doubly segregated. At this point, it is necessary to establish which of the two solutions shown in Figure 5c,d, (+, −, −, −, −) and (+, −, −, +, +), corresponds to a bilayer column.

**2.3.2. Calculation of the Number of Dendrons Forming the Inner and Outer Layers of Doubly Segregated Phases.** Table 2 summarizes the values of the number of dendrons forming the inner and outer layers of the bilayer assemblies, $\mu_{in}$ and $\mu_{out}$, respectively, calculated on the basis of the two new methodologies illustrated in Figure 6 and detailed in subsection 5.3 of the Supporting Information. Each of the two alternative methods uses one additional structural parameter extracted from molecular models, the length of the dendron, $\lambda$, for method A and the aliphatic region thickness, $\delta$, for method B. For the doubly segregated supramolecular structures, the values presented in Table 2 indicated that $\mu_{in}$ is always smaller than $\mu_{out}$, as expected on the basis of the mechanism illustrated in Scheme 3.

Therefore, the inner aliphatic region has a smaller total number of electrons than the outer aliphatic region. At the same time, the possibility that the inner confined aliphatic region can be locally more compact than the outer aliphatic region cannot be excluded. This in turn can generate a higher average electron density at the core than at the periphery. Therefore, in general, a bilayer structure can exhibit an electron density distribution with a value at the core that is lower than, comparable to, or higher than that at the periphery.

On the basis of this observation, the answer to the phase problem, presented in Figure 5c,d, is extracted from the systematic fits of the powder X-ray data obtained from models that have a core region containing $\mu_{in} = 0, 1, ..., 5, 6$ dendrons (Supporting Information, Tables ST4 and ST5). The fits for $\mu_{in} \leq 3$ converged to the phase solution (+, −, −, −, −) and matched relatively well the experimental amplitudes, but provided an unphysical small aromatic region. Therefore, the electron density of the aromatic region, $\rho_{aromatic}$, has larger than expected values, ranging from 0.6 $e^-$ Å$^{-3}$ for $\mu_{in} = 0$, to 0.55 $e^-$ Å$^{-3}$ for $\mu_{in} = 3$. The fits for $\mu_{in} = 5$ and 6 converged to the phase solution (+, −, −, +, +) matched better the experimental amplitudes and provided physical parameters within the expected range[7c,22] of $\rho_{aromatic} \approx 0.5\ e^-$ Å$^{-3}$ and $\rho_{aliphatic} \approx 0.3\ e^-$ Å$^{-3}$ (Figure 5d, Tables ST4 and ST5). Combining all the above, we conclude that the phase solution (+, −, −, +, +), shown in Figure 5d, provides the electron density map consistent with a bilayer hexagonal phase and that for this library of hybrid

---

(22) Turner, D. C.; Gruner, S. M. *Biochemistry* **1992**, *31*, 1340–1355.

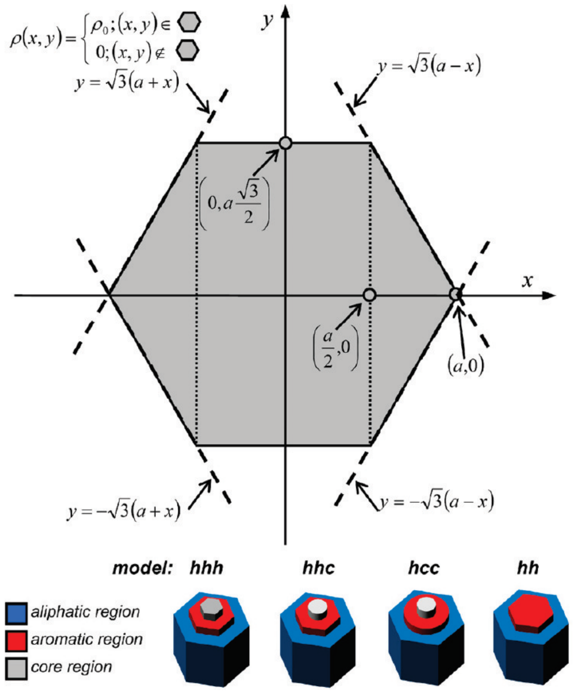

**Figure 7.** Geometric representation of the hexagonal distribution $\rho(x,y)$ and schematic of the models used in the powder XRD simulations. The equations defining the dashed boundary of the shaded domain are indicated.

dendrons the threshold between singly and doubly segregated columns is somewhere between 4.5% and 10.3% empty volume fraction. Therefore, none of the other investigated structures functionalized with $C_{12}H_{25}$ or dm8* alkyl chains (Schemes 1, 2) are expected to form hollow columns if their hypothetical empty volume fraction is larger than 10.3% because the strength of their aromatic interactions is either comparable or smaller and consequently cannot stabilize such a large hollow cavity.

**2.3.3. Simulation of the Powder X-ray Diffraction Data of Hollow, Nonhollow, and Singly and Doubly Segregated Polyhedral Columns Self-Organized into Hexagonal Phases.** The reconstructed electron density maps shown in Figure 5 demonstrate that the increase of the relative intensity of the higher order diffraction peaks is generated in part by the electron density variation within the supramolecular columns. This variation is from the higher value of the aromatic region to the lower one of the hollow center for singly segregated columns (Figure 5a) or of the inner aliphatic region for doubly segregated columns (Figure 5d). Furthermore, the shape of the high electron density region is very close to an ideal hexagon. Therefore, simulations of the X-ray powder diffractograms of the hexagonal phases with unusual amplification were calculated from the general equation of the scattering amplitude applied to the models shown in Figure 7:

$$F(\vec{q}) = \int \rho(\vec{r})\, e^{i\vec{q}\,\vec{r}}\, d\vec{r} \qquad (1)$$

Using the hexagonal distribution $\rho(x,y)$ defined in Figure 7, the appropriate integration limits of eq 1 are

$$\frac{F_{\text{hex}}(a, q_x, q_y)}{\rho_0} = \int_{-a}^{-a/2} dx \int_{-\sqrt{3}(a+x)}^{\sqrt{3}(a+x)} dy\, \cos(q_x x + q_y y) + \int_{-a/2}^{a/2} dx \int_{-a\sqrt{3}/2}^{a\sqrt{3}/2} dy\, \cos(q_x x + q_y y) + \int_{a/2}^{a} dx \int_{-\sqrt{3}(a-x)}^{\sqrt{3}(a-x)} dy\, \cos(q_x x + q_y y)$$

After integration, the scattering amplitude given by a hexagonal distribution is

$$F_{\text{hex}}(a, \rho_0, q_x, q_y) = \frac{4\rho_0}{q_x q_y} \sin\left(\frac{a}{2}q_x\right) \sin\left(\sqrt{3}\frac{a}{2}q_y\right) + \frac{2\rho_0}{q_y(q_x + \sqrt{3}q_y)}\left[\cos(aq_x) - \cos\left(\frac{a}{2}q_x - \sqrt{3}\frac{a}{2}q_y\right)\right] - \frac{2\rho_0}{q_y(q_x - \sqrt{3}q_y)}\left[\cos(aq_x) - \cos\left(\frac{a}{2}q_x + \sqrt{3}\frac{a}{2}q_y\right)\right] \qquad (2)$$

Finally, the calculated scattering amplitude of the hhh model shown in Figure 7, $F^{\text{hhh}}$, based on hexagonal distributions with constant electron density for the aliphatic ($\rho_{\text{aliph}}$), aromatic ($\rho_{\text{arom}}$), and core ($\rho_{\text{core}}$) regions, is given by

$$F^{\text{hhh}}(q_x, q_y) = F_{\text{hex}}(R_{\text{aliph}}, \rho_{\text{aliph}}, q_x, q_y) + F_{\text{hex}}(R_{\text{arom}}, \rho_{\text{arom}} - \rho_{\text{aliph}}, q_x, q_y) + F_{\text{hex}}(R_{\text{core}}, \rho_{\text{core}} - \rho_{\text{arom}}, q_x, q_y) \qquad (3)$$

The scattering amplitude, $F^{\text{hhc}}$, of the alternative hhc model shown in Figure 7, consisting of aliphatic and aromatic regions with hexagonal constant electron density distributions and a cylindrical core of constant electron density, is given by eq 4, with $F_{\text{cyl}}$ given by eq 5, deduced previously.[9f]

$$F^{\text{hhc}}(q_x, q_y) = F_{\text{hex}}(R_{\text{aliph}}, \rho_{\text{aliph}}, q_x, q_y) + F_{\text{hex}}(R_{\text{arom}}, \rho_{\text{arom}} - \rho_{\text{aliph}}, q_x, q_y) + F_{\text{cyl}}(R_{\text{core}}, \rho_{\text{core}} - \rho_{\text{arom}}, q_x, q_y) \qquad (4)$$

$$F_{\text{cyl}}(R, \rho, q_x, q_y) = 2\pi R^2 \rho \frac{J_1\sqrt{(q_x R)^2 + (q_y R)^2}}{\sqrt{(q_x R)^2 + (q_y R)^2}} \qquad (5)$$

The simulated X-ray powder diffraction amplitudes used in Figure 5 are presented in Figure 8 for the case of singly segregated polyhedral columns and in Table ST5 (Supporting Information) for the case of doubly segregated polyhedral columns. These simulations are based on eqs 3 and 4, following the procedure detailed in section 5.2 of the Supporting Information. The agreement between the experimental and fitted amplitudes is shown in Figure 8a for (6Np-3,4)12G1-$CO_2CH_3$ and in Figure 8b for (4Bp-3,4)12G1-$CO_2CH_3$for the hhh and hhc models. The amplitudes given by these two models fitted the experimental ones within the calculation error of 10−20%. Furthermore, Figure 5a illustrates the agreement of the electron density maps reconstructed from the experimental and hhc model fitted amplitudes for (4Bp-3,4)12G1-$CO_2CH_3$ and their agreement with the molecular model built on the basis of the fitted 14.8 ± 3.5 Å hollow region diameter. The small difference observed between the amplitudes fitted by the model with a circular (hhc model in Figure 7) versus polygonal (hhh model in Figure 7) core region is expected, considering the relatively limited number of Fourier components included in the analysis. On the other hand, the fitted amplitudes based on the hcc model with circular-shaped aromatic and core regions, exhibited a significantly larger deviation of the (21) diffraction peak amplitude, (hcc model fitted amplitudes indicated in Figure 8 by the green-colored tilted squares). Therefore, the simulations of the powder XRD data from Figures 5 and 8 demonstrated that the unusual amplification of the higher order diffraction peaks is correlated both with the presence of a low electron density region at the center of the columns and with the polygonal shape of the aromatic region. These two effects cannot

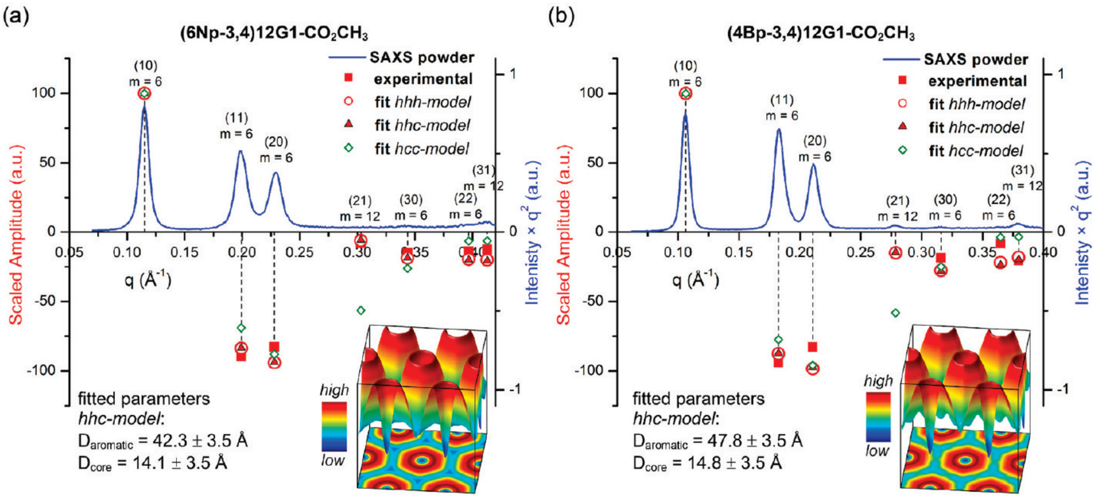

***Figure 8.*** SAXS powder data collected in the columnar hexagonal phase from (6Np-3,4)12G1-$CO_2CH_3$ (a) and (4Bp-3,4)12G1-$CO_2CH_3$ (b). Diffraction peak indexing and multiplicity, together with experimental (red squares) and fitted (red circles, red triangles, and green tilted squares) scaled amplitudes, are indicated. The two lower right insets depict the electron density maps, reconstructed from the experimental amplitudes, and their surface representation.

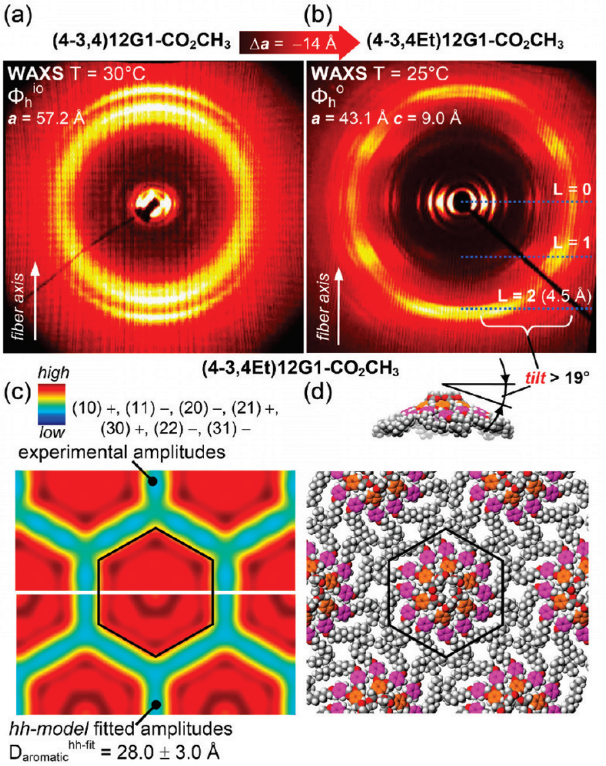

***Figure 9.*** WAXS patterns collected from the oriented fibers of (4-3,4)12G1-$CO_2CH_3$ (a) and (4-3,4Et)12G1-$CO_2CH_3$ (b). Relative electron density maps reconstructed from the experimental and fitted amplitudes (c) and molecular model (d) of (4-3,4Et)12G1-$CO_2CH_3$ in the $\Phi_h{}^o$ phase.

be separated. Hence, the parameters were fitted with larger error intervals of approximately ±3.5 Å.

**2.3.4. Singly Segregated Nonhollow Polyhedral Columns.** One of the most surprising results observed in the self-assembly of the first-generation benzyl dendritic esters is the unusual decrease of the lattice dimension of the columnar hexagonal phase upon the change of the apex group from 3,4 to 3,4Et. The analysis of the WAXS fiber patterns, shown in Figure 9a,b for the two structures, demonstrated that the unusual decrease of the lattice dimension of $\Delta a = -14$ Å is accompanied by the formation of long-range intercolumnar order and by a possible tilt-conformation[1q] of the (4-3,4Et)12G1-$CO_2CH_3$ dendron in the $\Phi_h{}^o$ phase. The possible tilt conformation shown in Figure 9d is also suggested by the comparison of the lattice dimension of $a = 43.1$ Å for the (4-3,4Et)12G1-$CO_2CH_3$ dendron with $a = 52.3$ Å for the corresponding (4-3,4Et)12G1-$CH_2OH$ dendron. In addition, the relative intensities of the higher order X-ray powder diffraction peaks of (4-3,4Et)12G1-$CO_2CH_3$, shown in Figure 1a, are at the highest levels observed thus far for any self-assembling benzyl ether dendron. The relative electron density maps (reconstructed from the experimental and from the hhh model fitted amplitudes via eq 3 with $R_{core} = 0$) shown in Figure 9c demonstrated that the (4-3,4Et)12G1-$CO_2CH_3$ dendron self-assembles into nonhollow polyhedral columns, presented in Figure 9d.

**2.3.5. From Hollow Polyhedral Columns to Nonhollow Bilayer Polyhedral Columns via Changes of the Dendron Alkyl Periphery.** The results discussed thus far revealed a complex correlation among the dendritic aromatic region, the apex building block, and the self-assembly process. Bilayer hexagonal and cubic phases were observed for all the dendrons with 3,4Et and 3,4Pr groups at the apex (Table 2) but not in the closely related (4Bp-3,4)12G1-$CO_2CH_2CH_2OCH_3$. The results presented in Figure 10 further expand this complexity: upon the functionalization of the (6Np-3,4)-R-G1-$CO_2CH_3$ dendron periphery with chiral chains (Schemes 1 and 2, R = dm8*), it was observed that the self-assembly preserved the pathway of forming a columnar hexagonal phase, but that the lattice dimension increased by 5 Å. This is unexpected considering that the length of the dendron was reduced (Figure 10a). Figure 10b compares the relative electron density distribution of the hollow singly segregated polyhedral columns of (6Np-3,4)12G1-$CO_2CH_3$ with the two possible solutions for (6Np-3,4)dm8*G1-$CO_2CH_3$. If the self-assembly process is not influenced by the change of the periphery, path II in Figure 10b, the diameters of the column and of the empty core region should decrease. On the other hand, if the self-assembly pathway is changed from singly to doubly segregated columns by the addition of the chiral centers, the diameters of the column and of the lower electron density core region should increase (path I in Figure 10b). Clearly, only the latter case is supported by the experimental data. Interestingly, wide angle oriented fiber X-ray diffraction data (Figure SF5, Supporting Information) demonstrated that the unusual formation of a bilayer columnar

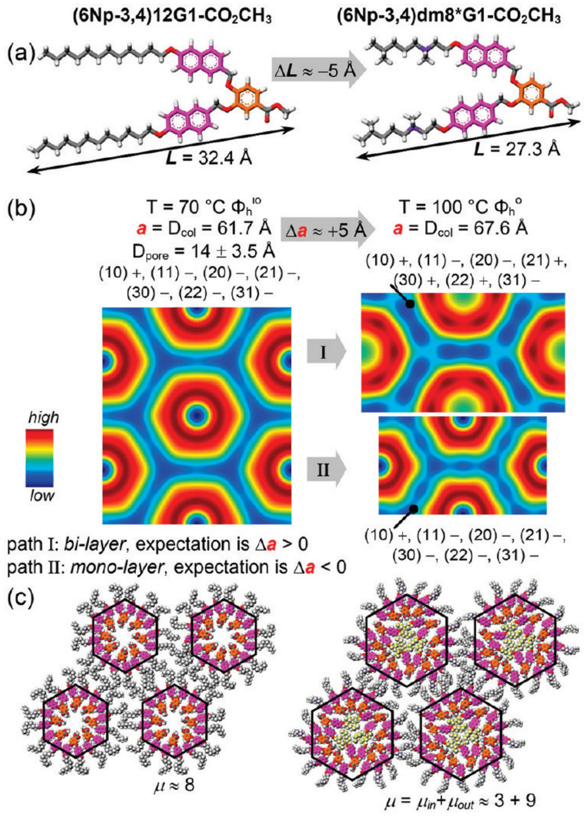

***Figure 10.*** Fully extended molecular models of the naphthyl methyl ether hybrid dendrons functionalized with achiral (left) and chiral (right) alkyl chains in an *all-trans* conformation (a). Corresponding reconstructed relative electron density distributions presented at scale (b) and the corresponding molecular models of the hollow singly segregated and nonhollow doubly segregated polyhedral columns (c).

hexagonal phase upon the addition of the chiral centers is accompanied by the formation of additional long-range intra- and intercolumnar correlations. The additional features observed in the XRD fiber pattern of the chiral dendron can be correlated with a possible dendron tilt conformation[1q] and also with the formation of a supramolecular dimer. Therefore, although the solid angle of the dendron was expected to decrease upon the change from achiral to chiral chains, the formation of additional long-range correlations suggests that the chiral dendron might have a different conformation. Because the assignment of these additional features observed in the fiber XRD patterns is not definitive, the exact changes of the 3-dimensional conformations of the dendrons, mediated by the addition of chiral centers, are not known. In the next section a second example of a bilayer phase induced via alkyl branching will be described.

These results, in combination with the data shown in Figures 1, 5, 9, and 10, illustrate a variety of polyhedral self-assembled structures with a comparable increase of the relative intensity of the higher order X-ray diffraction peaks. Analysis of the library of dendrons shown in Scheme 2 revealed the complexity of the process required to reconstruct the electron density maps and to assign the self-assembled structure as hollow or nonhollow and singly segregated or doubly segregated polyhedral supramolecular columns. Simulations of the XRD data combined with molecular models demonstrated that the significant enhancement of the higher order diffraction peaks of the hollow, nonhollow, or bilayer columnar hexagonal phases was generated by the polyhedral shape of the aromatic region and by the variation of the electron density from the higher value of the aromatic layer to the lower value of the inner aliphatic layer or of the empty core. At this point, it is necessary to elucidate why the aromatic region of all the structures that self-assembled into bilayer columns adopt a polyhedral shape.

**2.4. Analysis of the Cubic Phases Self-Organized from Polyhedral Vesicles.** The formation of bilayer vesicular phases is triggered by the addition of one or two methylenic units to the apex of the dendron (Table 1). The 3-dimensional reconstructed electron density distributions are shown in Figure 11b for the smallest, (4-3,4Pr)12G1-$CO_2CH_3$, and largest, (4Bp-3,4Pr)12G1-$CO_2CH_3$, first-generation dendrons investigated. The similarity of the high electron density regions to the Voronoi polyhedral representation of the $Pm\bar{3}n$ unit cell is remarkable. It is most probable that the mechanism that triggers the formation of polyhedral columns is also responsible for generating the polyhedral vesicles.

The at-scale comparison of the electron density maps of the plane $z = 0$ and of their corresponding profiles shown in Figure 11c,d illustrates the gradual increase of the size of the supramolecular clusters and the gradual decrease of the relative electron density at their centers. This gradual process follows the reduction of the solid angle of the dendron, generated by the increase of the length of the aromatic region. It is remarkable to what extent these small additions impact the change of the cluster size: an estimated 4 Å increase of the length of the unit (Figure 2, 36.7 Å [$L$ for (4Bp-3,4Pr)12G1-$CO_2CH_3$] − 32.7 Å [$L$ for (4-3,4Pr)12G1-$CO_2CH_3$] = 4 Å) translates into an 8-fold shift of the cluster size (Table 1, (221.5 − 155.9)/2 = 32.8 Å).

**2.4.1. Simulation of the X-ray Powder Diffraction Data of Polyhedral Doubly Segregated Vesicles.** The simulations of the X-ray powder diffraction data were performed via a new methodology (Figure 12), which was inspired by the similarity of the estimated shape of the aromatic region of the vesicles to the corresponding Voronoi polyhedral representation of the $Pm\bar{3}n$ lattice (Figure 11b). Using eq 1, the X-ray powder diffraction scattering amplitudes for this phase are given by

$$F(\vec{q}) = A\sum_{j=1}^{8}[F_j(\vec{q}, \rho_{\text{aliph}}, R_{\text{aliph}}) + F_j(\vec{q}, \rho_{\text{arom}} - \rho_{\text{aliph}}, R_{\text{arom}}) + F_j(\vec{q}, \rho_{\text{core}} - \rho_{\text{arom}}, R_{\text{core}})] \quad (6)$$

In eq 6 $A$ is the scaling factor, and the eight functions $F_j$ are given by

$$F_j(\vec{q}, \rho, \beta) = \rho\int\delta_j(\vec{r}, \beta)\, e^{i\vec{q}\cdot\vec{r}}\, d\vec{r} \quad (7)$$

The calculation of eq 7 was performed by multidimensional numerical integration after introduction of the function $\delta_j$. This function was deduced from the scaled Voronoi tessellation shown in Figure 12, and it is defined in eq 8, with $\vec{X}_i$ given by eq 9.

$$\delta_j(\vec{r}, \beta) = \begin{cases} 1, |\vec{r} - \vec{r}_j| \le |\vec{r} - \vec{X}_i(\vec{r}_i, \vec{r}_j, \beta)|, \forall X_i \in \Lambda, i \ne j \\ 0, |\vec{r} - \vec{r}_j| > |\vec{r} - \vec{X}_i(\vec{r}_i, \vec{r}_j, \beta)|, \forall X_i \in \Lambda, i \ne j \end{cases} \quad (8)$$

$$\vec{X}_i(\vec{r}_i, \vec{r}_j, \beta) = \beta\cdot\vec{r}_i + (1 - \beta)\vec{r}_j \quad (9)$$

In eqs 8 and 9, $\Lambda = \{(-0.5, -0.5, -0.5), ..., (0.25, 0, 0.5), ..., (1.5, 1.5, 1.5)\}$ is a set of the $Pm\bar{3}n$ lattice points that covers the range $\{-0.5 \le x \le +1.5, -0.5 \le y \le +1.5, -0.5 \le z \le +1.5, \}$ and $\vec{r}_j$ are the vectors to the center of the eight

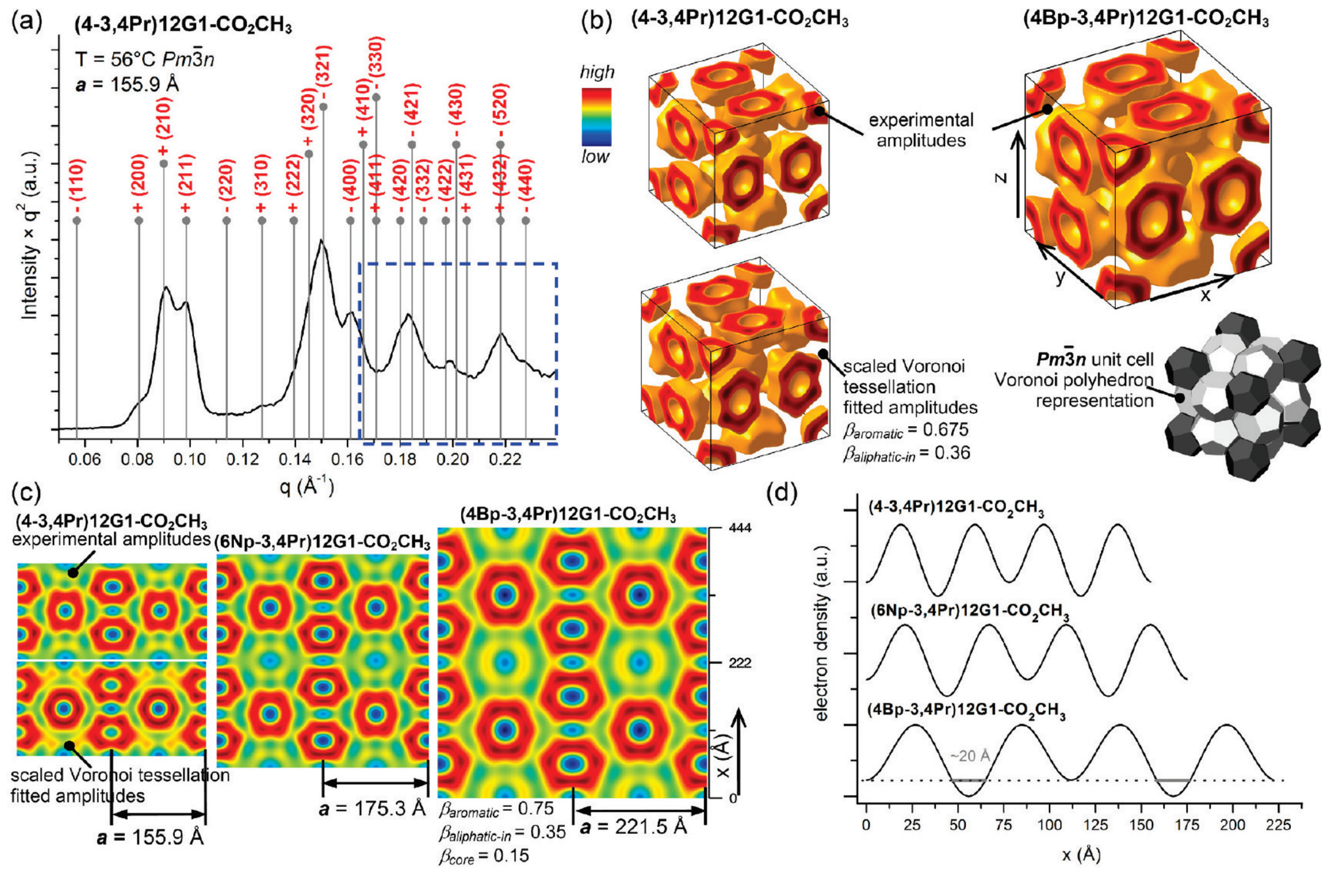

***Figure 11.*** SAXS powder diffraction data collected from (4-3,4Pr)12G1-$CO_2CH_3$ in the cubic phase (a). Reconstructed relative electron density distributions shown only for the high density regions (b). Reconstructed relative electron density maps of the plane $z = 0.5$ shown at scale (c). Relative electron density profiles of the $z = 0.5$ plane along the $x$ direction marked in panel c (d). In panel a, diffraction peak indexing and phases (+ or −) used in the electron density reconstructions are indicated, and the dashed rectangle indicates the region with overlapped diffraction peaks.

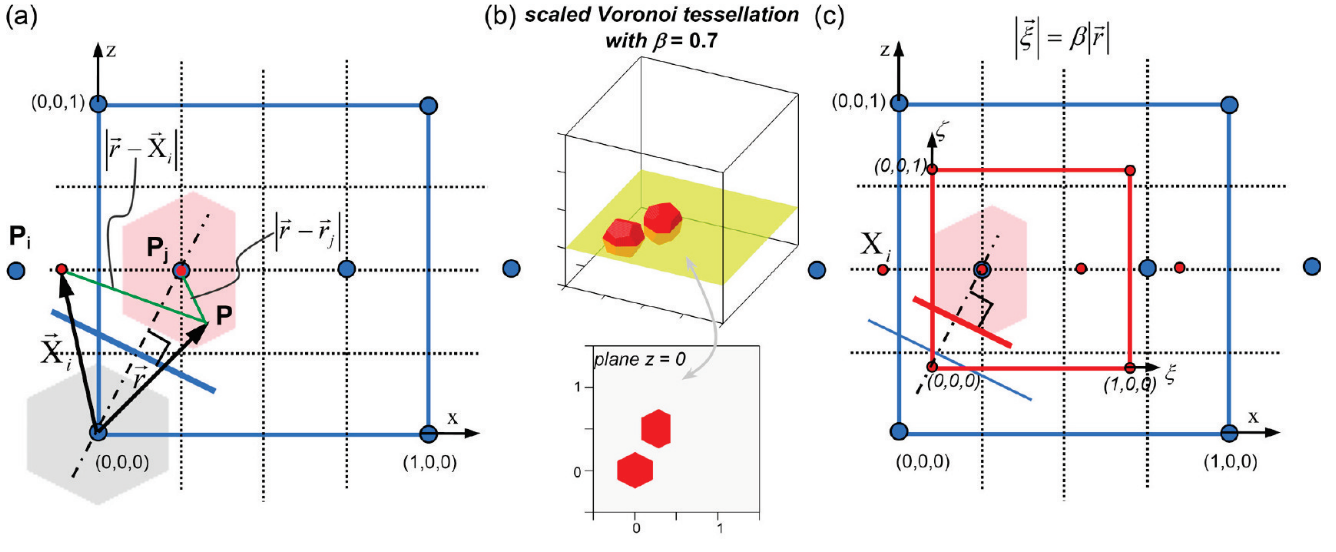

$$P \in V_j \text{ if } |\vec{r}-\vec{r}_j| \le |\vec{r}-\vec{X}_i|, \forall X_i \in \Lambda, i \neq j \text{ where } \Lambda = \{\text{set of lattice points } ● \equiv X_i\}, V_j\text{=scaled Voronoi polyhedron associated with the lattice point } P_j\text{, and } \vec{X}_i = \beta \cdot \vec{r}_i + (1-\beta)\vec{r}_j$$

***Figure 12.*** Geometric representation of the scaled Voronoi tessellation of the $Pm\bar{3}n$ cubic lattice. In (a) the unit cell is shown in normalized coordinates. In (b) the 3-dimensional representation of the scaled Voronoi tessellation is shown for $\beta = 0.7$ (for clarity only one center and one face polyhedron are shown). In (c) the spatial linear transformation used to calculate the scaled tessellation is shown for the lattice point $P_j = (0.25, 0, 0.5)$.

polyhedrons that form the basis of the $Pm\bar{3}n$ cubic lattice defined as $\{\vec{r}_j\} = \{(0, 0, 0), (0.5, 0.5, 0.5), (0.5, 0.25, 0), (0.5, 0.75, 0), (0.25, 0, 0.5), (0.75, 0, 0.5), (0, 0.5, 0.25), (0, 0.5, 0.75)\}$. For all the fits, the scale of the Voronoi tessellation is given by the parameter $\beta$, as illustrated in Figure 12. For example, the special case of $\beta = 1.0$ corresponds to the case when all the polyhedrons completely fill the unit cell, as illustrated by the Voronoi representation shown in Figure 11b.

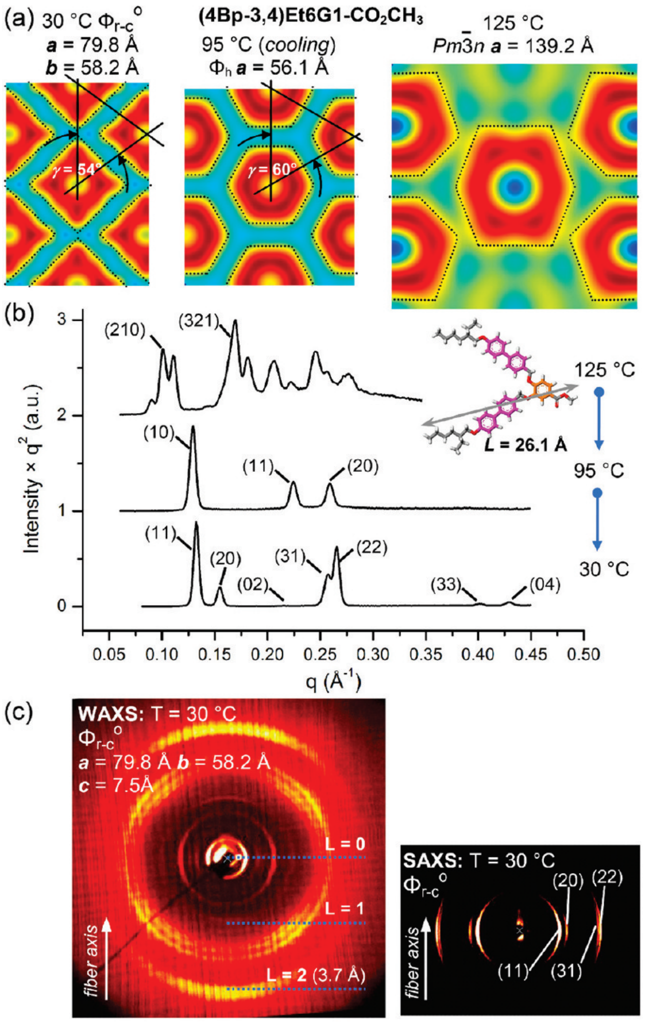

***Figure 13.*** Reconstructed relative electron density maps shown at scale (a), corresponding small-angle X-ray powder diffraction data collected upon cooling from the isotropic phase (b), and wide- and small-angle X-ray diffraction patterns collected in the $\Phi_{r\text{-}c}^{o}$ phase from the oriented fiber of (4Bp-3,4)Et6G1-$CO_2CH_3$ (c).

Simulations based on the scaled Voronoi tessellation methodology and eq 6, shown in Figure 11, demonstrated that the enhanced amplitudes are generated by a combination of the polyhedral shape of the clusters and by the variation of the electron density from the higher value of the aromatic region to the lower value of the inner aliphatic region. Furthermore, the intensity profiles of the biphenyl methyl ether hybrid dendrons with 3,4Et and 3,4Pr groups at the apex were consistent only with fits to a model that has an additional hollow center. It is most probable that the additional degree of freedom of the biphenyl aryl−aryl $sp^2$−$sp^2$ bond triggered a slightly different self-assembly mechanism. The corresponding benzyl ether and naphthyl methyl ether dendrons lack this additional conformational freedom. A relatively small torsion around the biphenyl aryl−aryl $sp^2$−$sp^2$ bond can significantly reduce the solid angle of the dendritic unit. This process can account for the observed increase of the lattice dimensions and of the higher order diffraction peaks' relative amplitudes for both columnar and cubic phases upon the change from naphthyl methyl ether to biphenyl methyl ether dendrons (Figure 1).

The agreement between the experimental and Voronoi scaled fitted amplitudes is illustrated in Figure 11 by the reconstructed relative electron density distributions. Figure 11b compares the experimental and simulated high electron density 3-dimensional distributions of the (4-3,4Pr)12G1-$CO_2CH_3$, with the complete distributions detailed in Figure 11c for the plane $z = 0.5$. The fitted parameters $\beta$ are also indicated for the smallest and largest structures: (4-3,4Pr)12G1-$CO_2CH_3$ and (4Bp-3,4Pr)12G1-$CO_2CH_3$. In both cases, the fitted parameters provided a good estimate for the thickness of the outer aliphatic layer: $(1 - \beta_{\mathrm{aromatic}}) \times 155.9$ Å/4 = 12.7 Å and $(1 - \beta_{\mathrm{aromatic}}) \times 221.5$ Å/4 = 13.9 Å, respectively. These two values were calculated in the direction parallel to the close contact of the assemblies from the face of the $Pm\bar{3}n$ lattice.

The assessment of a relatively small hollow center with a diameter of ~20 Å was based on the reconstructed electron density distributions shown in Figure 11d and on the Voronoi fits presented in Supporting Information Figure SF10. This small hollow center translates to an empty volume fraction of less than 1% from the supramolecular structure: $8(4\pi/3)(20\ \text{Å}/2)^3/(221.5\ \text{Å})^3 = 0.31\%$. In addition, the molecular modeling shown in Figure 2 in combination with the $Pm\bar{3}n$ lattice parameters of the three structures presented in Figure 11c,d also supports the idea that the sharpest dendron, (4Bp-3,4Pr)12G1-$CO_2CH_3$, self-assembles into a hollow vesicle, as follows. Assuming that the change of the aromatic region structure does not significantly change the density of the aliphatic region and that the vesicles self-assembled from (4-3,4Pr)12G1-$CO_2CH_3$ have a very small hollow center, we can extrapolate the $Pm\bar{3}n$ cubic lattice dimension from the length of the dendritic units shown in Figure 2. Upon the change from (4-3,4Pr)12G1-$CO_2CH_3$ to (6Np-3,4Pr)12G1-$CO_2CH_3$ the lattice dimension is expected to be 155.9 Å[(4-3,4Pr)12G1-$CO_2CH_3$] + 8(34.9 − 32.7) Å = 155.9 + 17.6 Å = 173.5 Å. The multiplication factor 8 accounts for the fact that two bilayer assemblies span through one side of the $Pm\bar{3}n$ unit cell and that four dendrons span through one bilayer assembly. The calculated values are slightly overestimated because they are not corrected for interdigitation. The experimental value of $a(Pm\bar{3}n) = 175.3$ Å is almost 2 Å larger than the expected value. This small difference suggests that the vesicle self-assembled from (6Np-3,4Pr)12G1-$CO_2CH_3$ has a hollow region only if those self-assembled from (4-3,4Pr)12G1-$CO_2CH_3$ are hollow. On the other hand, upon the change from (6Np-3,4Pr)12G1-$CO_2CH_3$ to (4Bp-3,4Pr)12G1-$CO_2CH_3$ the expected lattice dimension is 175.3 Å + 8(36.7 − 34.9) Å = 175.3 + 14.4 Å = 189.7 Å. This value is 31.8 Å smaller than the experimental value of $a(Pm\bar{3}n) = 221.5$ Å. Therefore, this significant difference suggests that the vesicles self-assembled from (4Bp-3,4Pr)12G1-$CO_2CH_3$ are hollow.

**2.5. Principles of Formation of Polyhedral Singly and Doubly Segregated Columns and Vesicles.** The self-assembly process of the hybrid biphenyl methyl ether dendron functionalized with a second type of branched alkyl periphery, (4Bp-3,4)Et6G1-$CO_2CH_3$, is summarized in Figure 13. This is the only dendritic architecture containing a 3,4 group at the apex that exhibits a bilayer cubic phase. Interestingly, no cubic phase was observed upon the self-assembly of this dendron functionalized with dm8* chiral chains.[23] The biphenyl methyl ether hybrid (4Bp-3,4)Et6G1-$CO_2CH_3$ dendron self-assembles at low temperatures into a centered rectangular phase with a unique characteristic. This is the only centered rectangular phase with an angle between the *a* and *b* directions of the lattice smaller

---

[23] Kim, A. J.; Kaucher, M. S.; Davis, K. P.; Peterca, M.; Imam., M. R.; Christian, N. A.; Levine, D. H.; Bates, F. S.; Percec, V.; Hammer, D. A. *Adv. Funct. Mater.* **2009**, *19*, 2930–2936.

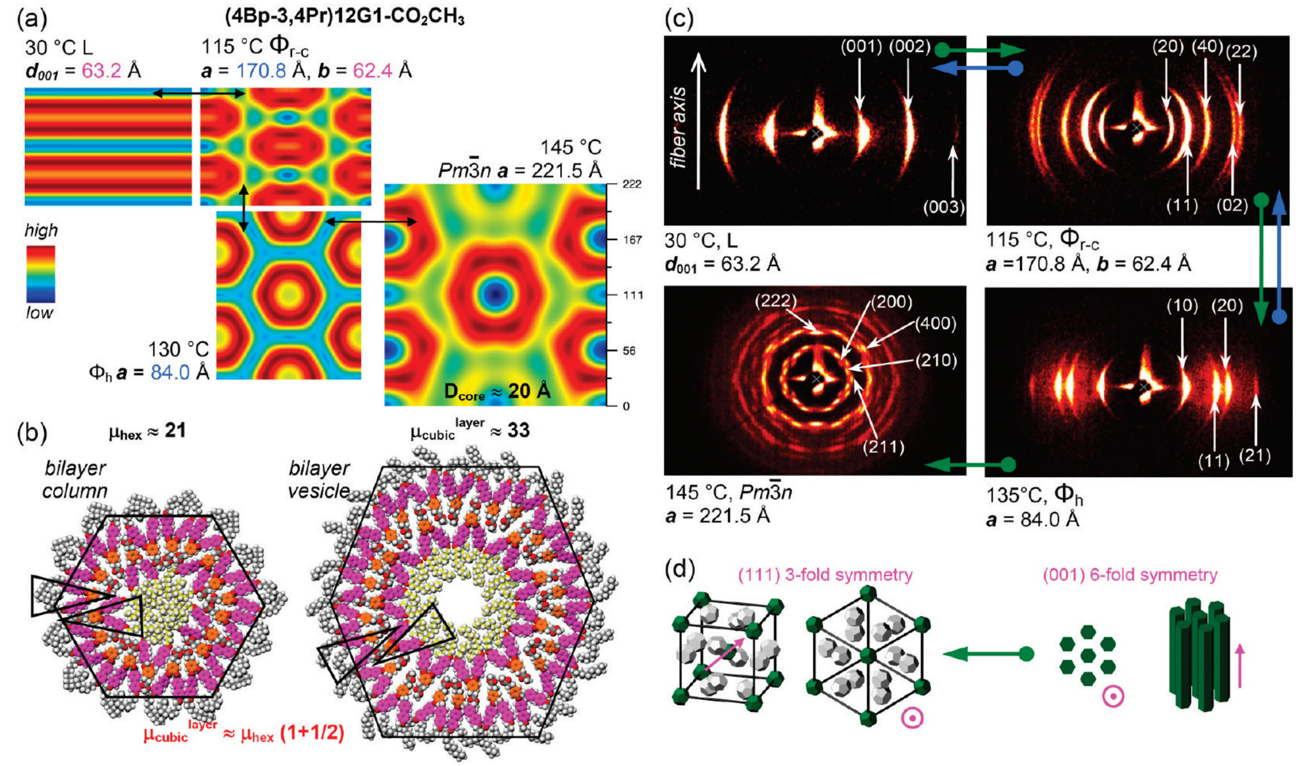

***Figure 14.*** Reconstructed relative electron density maps shown at scale (a) and molecular models of the column and vesicle cross-section (b). Small-angle X-ray diffraction patterns collected from the oriented fiber of (4Bp-3,4Pr)12G1-$CO_2CH_3$ indicating the reversible epitaxy among lamellar, centered rectangular, and hexagonal phases and the irreversible epitaxy upon the transition from hexagonal to cubic (c). Schematic of the $(001)_{\text{hexagonal}}-(111)_{\text{cubic}}$ epitaxy (d).

than the special value of 60° (Table 1; Supporting Information, Table ST2). The $\gamma$ angle was measured in the triangle formed by the centers of three first-order neighboring columns, Figure 13a. This latter value is achieved in the case of $2b = a \cos 60°$, when the centered rectangular lattice reduces to the particular case of the hexagonal lattice (Figure 13a). In general, centered rectangular phases are expected to exhibit an angle $\gamma$ larger than 60° because the close contact direction of the supramolecular columns is expected to be perpendicular to their long-axis direction, as shown, for example, in the electron density map from Figure 14a. These two observations suggest a complex correlation of the dendron periphery and the formation of polyhedral and bilayer phases for the case of the (4Bp-3,4)Et6G1-$CO_2CH_3$ hybrid dendrons.

A closer inspection of the lattice parameters and of the relative electron density maps reconstructed for the (4Bp-3,4Pr)12G1-$CO_2CH_3$ dendron presented in Figure 14 revealed the thermally induced changes in the structure that trigger a complex phase diagram. At low temperatures the dendron self-assembles into a bilayer lamellar ordered phase, with a double layer thickness $d_{001} = 63.2$ Å. With an increase of the temperature above 90 °C (Figure 4), the rotational energy barriers of some of the bonds are comparable with the thermal energy and the dendrons tend to pack their aromatic regions closer together by forming asymmetric columns, while preserving the thickness of the lamellar phase bilayer ($b_{\text{centered rectangular}} = 62.4$ Å is comparable with $d_{001} = 63.2$ Å of the low-temperatures lamellar phase). Upon increasing the temperature above 119 °C, the structures minimize further their aromatic free energy by forming the more symmetric bilayer columns of the hexagonal phase, while preserving upon this transition the longer column diameter of their low-temperature centered rectangular phase ($a_{\text{centered rectangular}}/2 = 170.8/2 = 85.4$ Å is comparable with $a_{\text{hexagonal}} = 84.0$ Å). The process described thus far involves in-plane small translations and rotations of the dendrons. This mechanism was confirmed by the reversible epitaxial correlations presented in Figure 14c,d. The most complex process occurs when the temperature exceeds 139 °C during the formation of the dendritic vesicles. At this temperature, the thermal energy is at the level that the structure departs from the 2-dimensional taperlike conformation, forming a 3-dimensional conelike conformation, with the conformation of the alkyl chains predominantly controlling this process.

While the reversible epitaxial correlations illustrated in Figure 14c,d are not unusual, the irreversible $(001)_{\text{hexagonal}}$-to-$(111)_{\text{cubic}}$ epitaxy is remarkable. Although its direction is explained in Figure 14d by the preservation of the supramolecular packing rotational symmetry, such an effect was seen only in a few dendritic structures.[1t] The WAXS diffraction data, collected in the hexagonal and cubic bilayer phases, exhibit diffuse meridional features positioned at the average alkyl chain−chain correlation distance that indicate that the alkyl chains have a liquidlike conformational freedom. Therefore, the hexagonal-to-cubic epitaxy can be explained only by cluster-to-cluster interactions and by the conservation of some of the hexagonal phase polyhedral faces. In other words, the thermally induced supramolecular shape change follows the path of minimum required energy provided by the minimum rotation and translation of the units.

Figure 15 summarizes the combined analysis of the self-assembly and self-organization process of the amphiphilic dendrons that is updated with the bilayer polyhedral structures discovered in this study. In general, the equilibrium configuration of any self-assembled system is achieved when the free energy is at the minimum. In most self-assembled supramolecular dendrimers, the equilibrium configuration corresponds to the

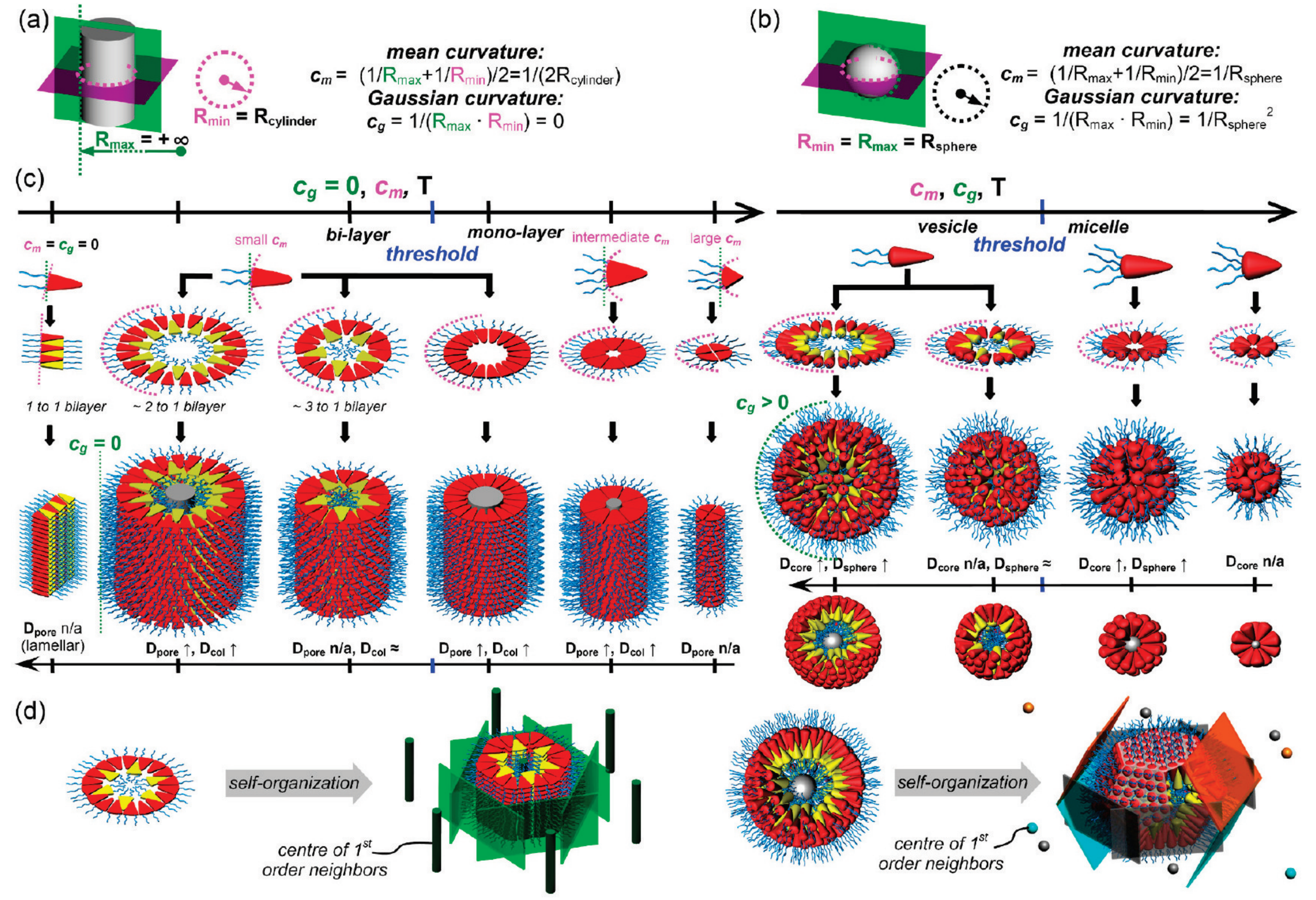

***Figure 15.*** Definition of the mean $c_m$ and Gaussian $c_g$ curvatures for a cylinder (a) and a sphere (b), where $R_{min}$ and $R_{max}$ are, respectively, the minimum and maximum possible values of the radii of the curve obtained by intersecting an arbitrary plane and the corresponding object. Mechanism of self-assembly into singly and doubly segregated assemblies (c) and of their self-organization into polyhedral-shaped supramolecular columns and vesicles (d). In (c) the schematic follows from left to right the increase of $c_m$, $c_g$, and temperature, separated for the case of the tapered dendron (left, $c_g = 0$) and the conical dendron (right, $c_g > 0$). The two curvatures of the surface of the supramolecular assemblies, $c_m$ and $c_g$, are represented by the dotted lines colored in pink and green, respectively, illustrating that a "sharp" dendron self-assembles into a cluster with small curvature (or alternatively large radii) and a "wide" dendron self-assembles into a cluster with large curvature (or alternatively smaller radii).

close-packing configuration illustrated in Figure 15c. This is valid in the conditions when the dominant intramolecular and intermolecular short-range dipolar interactions achieve their maxima by close-packing groups of covalently bonded atoms of similar species and spatial configurations. In this respect, the phase diagram shown in Figure 15c does not take into account a number of specific interactions, such as ionic or H-bonding, that can inhibit the formation of bilayer columns and spheres. At the same time, the formation of close-packing configurations can be viewed as following the minimization of the outer surface free energy of the assemblies, demonstrated previously.[24] Therefore, in Figure 15a,b two special surfaces are shown, cylindrical and spherical, to illustrate the definition of the mean ($c_m$) and Gaussian ($c_g$) curvatures. The dendritic building block is schematically represented by a taper, when $c_g = 0$, and by a cone, when $c_g > 0$. In Figure 15c, from left to right, the temperature, mean curvature, and Gaussian curvature, separated for systems with zero and nonzero Gaussian curvatures, $c_g$, increase.

The dependence from Figure 15 corresponds to both thermal architectural changes, because the increase of $c_m$ and of $c_g$ can be generated by an increase of temperature or by direct changes of the primary structure of the dendron. With the exception of the predicted hollow bilayer columnar structures, all the other structures were observed in the proposed order, in the library of hybrid dendrons investigated here or in other dendritic libraries.[7c,9] For clarity, Figure 15c illustrates the self-assembly process for the case when the cluster-to-cluster correlations are negligible. For example, this corresponds to self-assembly in dilute solutions. Figure 15d illustrates the result of the self-assembly and self-organization process when the supramolecular cluster-to-cluster correlations are not neglected. Upon "clustering", the network of short-range van der Waals attractive interactions between the periphery of the assemblies generates planar boundaries with their first-order neighboring clusters.

A variety of classes of structures forming faceted vesicles[8,25,26] and polygonal sheets[27] have been reported previously. In comparison with the dendritic polyhedral-shaped structures presented here, their formation was sometimes attributed to a possible crystallization of the surfactant film[25a] and to quenching.[25b] Interestingly, in at least two cases[26] polygonal structures have been observed to spontaneously form in closely packed clusters. These two examples are in agreement with our

---

(24) (a) Ziherl, P.; Kamien, R. D. *Phys. Rev. Lett.* **2000**, *85*, 3528–3531. (b) Ziherl, P.; Kamien, R. D. *J. Phys. Chem. B* **2001**, *105*, 10147–10158. (c) Bates, F. S.; Fredrickson, G. H. *Annu. Rev. Phys. Chem.* **1990**, *41*, 525–527. (d) Matsen, M. W.; Bates, F. S. *Macromolecules* **1996**, *29*, 10914–1098. (e) Matsen, M. W.; Bates, F. S. *J. Chem. Phys.* **1997**, *106*, 2436–2448.

***Scheme 4.*** Correlation between the Structure of the Dendrons and the Shape of Their Supramolecular Assemblies

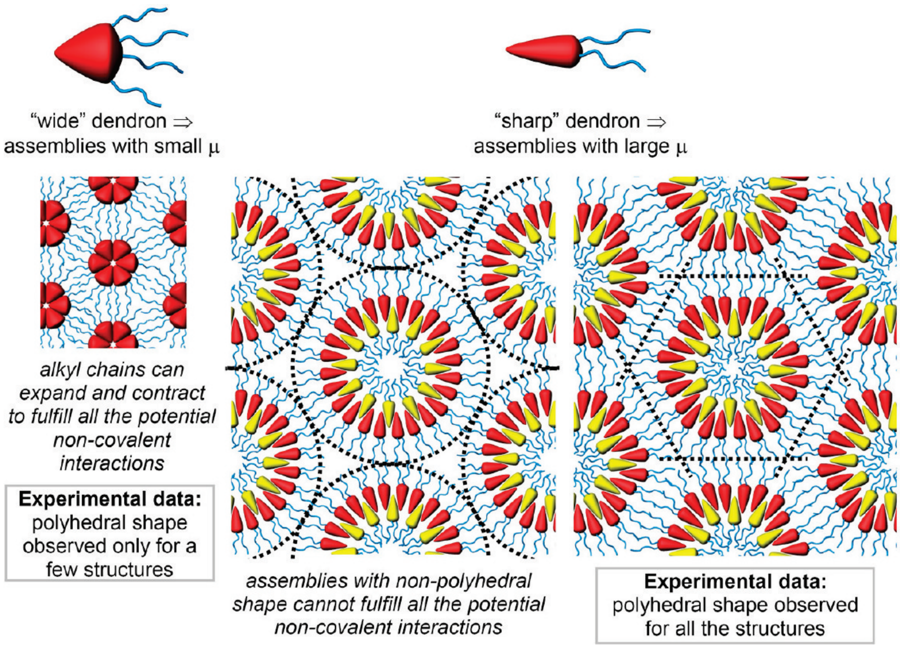

hypothesis that the supramolecular cluster-to-cluster interactions are the dominant factor in templating the polyhedral-shaped dendritic structures.

The supramolecular dendrimers tend to adopt shapes closer and closer to that of the idealized polyhedra templated by their self-organization, but this process depends on the number of dendrons, $\mu$, forming the assemblies. In general, a relatively large $\mu$ is required to observe supramolecular assemblies with well-defined close-to-planar boundaries (Scheme 4). For example, recent work elucidated the formation of spherical and oblate spherical supramolecular assemblies from a library of dendrons containing a carboxylic acid at their apex.[1s] Because for this library the number of dendrons forming the supramolecular assemblies was smaller than 12, the two shapes reported previously can be considered just rough approximations of the two types of Voronoi polyhedra present in the $Pm\bar{3}n$ lattice. Whereas in the case of the columnar and cubic bilayer phases reported in Table 1, the number of dendrons forming the doubly segregated supramolecular structures is always sufficiently large such that the assemblies adopt shapes that are much closer to the that of the idealized polyhedra templated by their self-organization, as illustrated in Scheme 4. Furthermore, in the case of the singly segregated phases reported in Table 1, polyhedral-shaped structures were observed only for hollow structures, which are also assembled from a larger number of dendrons,[7c,9] and in the two special cases discussed, (4-3,4Et)12G1-$CO_2CH_3$ and (4Bp-3,4)Et6G1-$CO_2CH_3$. Therefore, the mechanism proposed in Figure 15 elucidates why polyhedral structures are omnipresent in the bilayer cubic and columnar phases presented here. All the doubly segregated structures have as an intrinsic characteristically large $\mu$, due to the fact that their formation requires small $c_m$ and $c_g$.

## 3. Conclusions

The synthesis and structural analysis of three libraries of first-generation hybrid self-assembling dendrons revealed unprecedented supramolecular structures and pathways to self-assembly and self-organization. Dendrons that self-assemble into hollow and nonhollow polyhedral-shaped singly and doubly segregated aliphatic−aromatic supramolecular columns and vesicles were discovered. The mechanism of assembly of these new bilayer structures was shown to follow similar pathways that lead to the formation of cellular membranes. In the case of the dendritic bilayer columns and vesicles, the hydrophobic−hydrophilic interaction, which mediates the formation of cellular membranes, was replaced by a complex network of supramolecular interactions that templates an outer layer with small curvature determined by the solid angle of the dendron and an inner layer that interdigitates with the outer layer. The significant difference between the polygonal shape of the bulk dendritic bilayer supramolecular structures and that of the biological vesicles assembled in water is determined by the supramolecular cluster-to-cluster correlations. These correlations dominate the self-organization process of the doubly segregated supramolecular dendrimers. In the water phase of the cellular membranes the cluster-to-cluster correlations are negligible, and therefore most of them are globular rather than polyhedral. In addition, this study provided experimental data needed to elaborate a detailed mechanism of the self-assembly and of self-organization of supramolecular dendrimers into singly and doubly segregated phases. This mechanism predicts new supramolecular organizations and explains unusual changes of the internal packing of the supramolecular structures observed at high temperature, from singly segregated columns to doubly segregated vesicles and from doubly

---

(25) (a) Antunes, F. E.; Marques, E. F.; Gomes, R.; Thuresson, K.; Lindman, B.; Miguel, M. G. *Langmuir* **2004**, *20*, 4647–4656. (b) Raspaud, E.; Pitard, B.; Durand, D.; Aguerre-Chariol, O.; Pelta, J.; Byk, G.; Scherman, D.; Livolant, F. *J. Phys. Chem. B* **2001**, *105*, 5291–5297.

(26) (a) Borne, J.; Nylander, T.; Khan, A. *J. Phys. Chem. B* **2002**, *106*, 10492–10500. (b) Jung, H. T.; Coldren, B.; Zasadzinski, J. A.; Iampietro, D. J.; Kaler, E. W. *Proc. Natl. Acad. Sci. U.S.A.* **2001**, *98*, 1353–1357.

(27) Li, Z. B.; Hillmyer, M. A.; Lodge, T. P. *Nano Lett.* **2006**, *6*, 1245–1249.

segregated columns to doubly segregated hollow vesicles. The principles of the self-assembly process into doubly segregated structures provide access to the design of complex supramolecular organizations that can be used for applications such as molecular containers and polyhedral nanoparticles and for mimicking in bulk complex biological tubes and vesicles.

**Acknowledgment.** Financial support by the National Science Foundation (Grants DMR-0548559 and DMR-0520020) and the P. Roy Vagelos Chair at the University of Pennsylvania is gratefully acknowledged.

**Supporting Information Available:** Experimental procedures with complete spectral, structural, and retrostructural analysis and complete ref 8. This material is available free of charge via the Internet at http://pubs.acs.org.

JA104432D